3-23-2017

Transient Nonlinear Optical Properties of Thin Film Titanium Nitride

SarahKatie Thomas

TRANSIENT NONLINEAR OPTICAL PROPERTIES OF THIN FILM TITANIUM NITRIDE

THESIS

SarahKatie Thomas, Civ

AFIT-ENP-MS-17-M-106

DEPARTMENT OF THE AIR FORCE
AIR UNIVERSITY

AIR FORCE INSTITUTE OF TECHNOLOGY

Wright-Patterson Air Force Base, Ohio

AFIT-ENP-MS-17-M-106

TRANSIENT NONLINEAR OPTICAL PROPERTIES OF THIN FILM TITANIUM NITRIDE

THESIS

Presented to the Faculty

Department of Physics

Graduate School of Engineering and Management

Air Force Institute of Technology

Air University

Air Education and Training Command

in Partial Fulfillment of the Requirements for the

Degree of Master of Science in Materials Science

SarahKatie Thomas, B.S.

Civ

March 6, 2017

AFIT-ENP-MS-17-M-106

TRANSIENT NONLINEAR OPTICAL PROPERTIES OF THIN FILM TITANIUM NITRIDE

SarahKatie Thomas, B.S.
Civ

Committee Membership:

Manuel Ferdinandus, PhD
Chair

Amber Reed, PhD
Member

Larry Burggraf, PhD
Member

AFIT-ENP-MS-17-M-106

Abstract

The objective of this thesis is to measure the transient nonlinear properties of thin film titanium nitride (TiN), using the beam deflection characterization technique. The thin films are made at the Air Force Research Lab by controllably unbalanced reactive magnetron sputtering.

Transition metal nitrides, specifically TiN, are used widely in industry because of their unique properties, including extreme hardness and high damage threshold. The properties of thin film transition metal nitrites are dependent on the crystallinity of the thin film, which can be influenced by substrate and deposition method. This durability and tunability are assets in applications such as sensor protection and all optical computing.

The TiN thin films do not exhibit instantaneous (femtosecond time scale) electronic responses, which were observed in previous transient nonlinear optical measurements of thin film TiN. The thin films measured in this work are epitaxial growth, while the thin films measured in the previous work were not, which could explain this discrepancy.

The materials exhibit long (nanosecond time scale) responses, consistent with both semiclassical and phenomenological two temperature models. All TiN thin films exhibit two nonlinear absorption and two nonlinear refraction relaxations.

Two substrates, sapphire (Al_2O_3) and magnesium oxide (MgO), are investigated. A single deposition parameter, deposition power, is investigated. The substrate does not significantly affect the nonlinear optical properties, but deposition parameter affected the nonlinear refraction.

Acknowledgments

I would like to thank Maj. Manuel Ferdinandus for his guidance and patience; Dr. Larry Burggraf for his help from the day I arrived at AFIT to long into the future; and Dr. Amber Reed for both synthesizing these materials and kindness answering my many questions.

Special thanks to Dr. Jennifer Reed who taught me the beam deflection technique (and re-taught, and re-taught and re-taught); and Lt. Brady Gough, who was a pleasure to share a lab with. Best of luck to both in future adventures.

As always, thank you to my family. Whether it was middle school science fair projects, or a Masters thesis, you have consistently encouraged and supported me.

SarahKatie Thomas

Table of Contents

Page

Page

List of Figures

Figure Page

List of Tables

TRANSIENT NONLINEAR OPTICAL PROPERTIES OF THIN FILM TITANIUM NITRIDE

I. Introduction

1.1 Chapter Overview

This chapter will discuss the objectives for research, the motivation behind the research, and briefly discuss the background and methodology.

The goal of this work is to characterize the nonlinear optical (NLO) properties of thin film titanium nitride (TiN, tinite) using the beam deflection technique.

1.2 Objective

The objective of this thesis is to gain a better understanding of the transient nonlinear properties of thin film TiN. The properties of thin film transition metal nitrites, such as TiN, are dependent on the chemical structure of the thin film, which can be influenced by substrate and deposition method. Substrates investigated in this work are (001)-oriented cubic magnesium oxide (MgO, magnesia) and (0001)-oriented trigonal sapphire (Al_2O_3). A single deposition parameter, deposition power, will be investigated.

The specific research objectives are:

1. Measurements of the time dynamics of the NLO properties of TiN
    - Beam deflection NLO measurements of TiN
    - Determine if the mechanisms are that of a metal, semiconductor, or a combination of the two

2. Measure the effect of substrate on the NLO properties of TiN

   - Beam deflection NLO measurements of TiN on MgO
   - Beam deflection NLO measurements of TiN on Al_2O_3
   - Compare the NLO properties of TiN on Al_2O_3 to the NLO properties of TiN on MgO

3. Measure the effect of deposition power on the NLO properties of TiN

   - Beam deflection NLO measurements of TiN on MgO, 50 W
   - Beam deflection NLO measurements of TiN on MgO, 100 W
   - Compare the NLO properties of TiN on MgO, 50 W to the NLO properties of the TiN on MgO, 100 W

To meet these objectives, three samples are required, as listed in Table 1.1.

Thin Film	**Substrate**	**Deposition Power**
TiN	MgO	50 W
TiN	Al_2O_3	50 W
TiN	MgO	100 W

Table 1.1. Samples

1.3 Nonlinear Optical Properties

A material's optical properties describe how light behaves when incident on that material. The index of refraction (n) is the material property which describes how the incident light will refract, or bend. The absorption coefficient (α) is the material property which describes how light is absorbed by the material.

For traditional light sources, from a reading light to the sun, these properties are independent of the light's intensity. Intensity is power per unit area, with units

W/m^2. For very intense light, such as from a laser, the intensity of the light alters the material's properties, and thereby alters the absorption and refraction of the light. The study of this phenomenon is called nonlinear optics, and these properties are called nonlinear optical (NLO) properties. Materials with strong nonlinear optical properties may be called nonlinear optical materials.

1.4 Motivation

An important consequence of nonlinear optics is that light can effectively be used to manipulate light. A flashlight beam will have no effect on the light from another flashlight. But given the correct material, a laser can be used to change the material's optical properties, which will change how that material bends and absorbs other light.

Nonlinear optical materials are potentially useful in the future of computing and for protecting the military's growing fleet of sensors. Bringing these applications to reality may be be a long and iterative process. Engineers who wish to manipulate light using the NLO properties of materials and engineers whose products will be exposed to high irradiances must first understand how these NLO properties can be manipulated. As such, NLO characterization is an important early step.[7]

1.4.1 Imagining Protection

The United States military has an ever-growing, "portfolio of electro-optical sensors and related technology for intelligence, surveillance, and reconnaissance (ISR), targeting and situation awareness for manned, remotely piloted, and autonomous aircraft."[8] The United States' adversaries are constantly developing ways to thwart these capabilities. High power lasers can temporarily blind a system and, more importantly, cause permanent damage.

Nonlinear materials may offer protection for these valuable systems through optical limiting. The ideal material for this application would have small linear absorption, large NLO properties, and a high damage threshold.

An ideal optical limiter will act as a low pass intensity filter, allowing low intensity light to pass unaltered, and either absorbing or redirecting high intensity light. A material with large nonlinear absorption will be able to absorb this high intensity light. Though straightforward, this is often the less practical approach. A material with large nonlinear refraction will be able to unfocus and redirect the high intensity light, as shown in Figure 1.1.

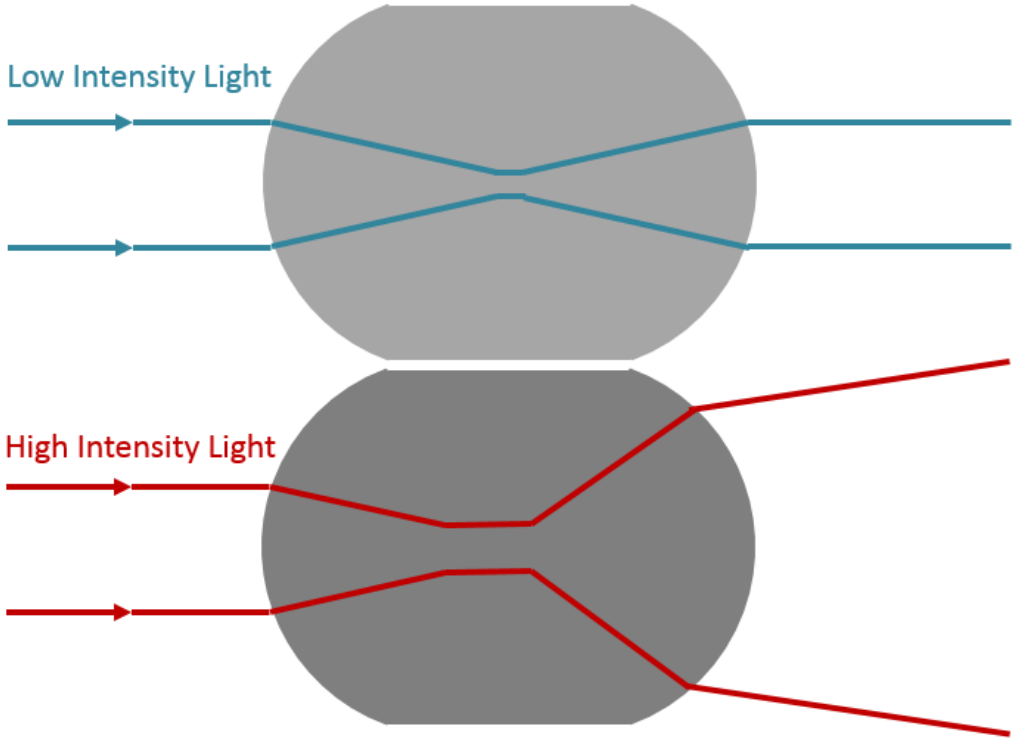

Figure 1.1. The grey lens is a material with large nonlinear refraction. Low intensity light, shown in blue, is allowed to pass unaffected. High intensity light, shown in red, is altered. Adapted from Stryland.[1]

1.4.2 All Optical Computing

Current computing works by manipulating electrons. Hence, the nomenclature "electronics." Electrons are manipulated by electric fields, which easy to manipulate down to the nanosecond scale. The optical material properties of nonlinear materials can be manipulated on a sub-femtosecond time scale, allowing for the ultrafast manipulation of photons. Since photons move more quickly than electrons, an optical computer would be orders of magnitude faster than an electronic computer. Quantum tunneling currently limits how small an electronic computer can be. Optical computing also avoids the problem of quantum tunneling, which currently puts a lower limit on the size of electronics. Furthermore, photon entanglement could be

exploited to make optical computers even more powerful. Current estimates predict that a working optical computer would have least three orders of magnitude more bandwidth than modern computers, while being even smaller. [7]

One obstacle to creating such a computer is finding nonlinear materials that are able to withstand the irradiance required to sufficiently manipulate the optical properties of the material in order to sufficiently manipulate the photons. This need could be fulfilled by materials that can withstand very high irradiances or materials that have stronger nonlinear optical properties, requiring relatively weaker irradiances.[7]

1.5 Beam Deflection Technique

The beam deflection technique is a method for measuring NLO properties. It has the benefit of measuring the NLO response as a function of time delay, providing temporal information other methods do not.

The beam deflection technique uses a strong pump beam to manipulate the material properties of a sample. The change in these material properties is measured by a weaker probe beam. Changes in deflection and intensity of the probe beam are collected by a detector. By moving the probe beam in time (by means of a mechanical delay stage) the nonlinear refraction and nonlinear absorption may be measured as a function of time. [7]

1.6 Overview

- Chapter I: States the objective of this thesis, establishes the motivation, and briefly discusses the background and methodology
- Chapter II: Discusses the theory presented in relative literature
- Chapter III: Describes the methodology used for this research

- Chapter IV: Presents the results
- Chapter V: Draws conclusions, and discusses recommendations for future research

II. Background

2.1 Chapter Overview

This chapter begins with a broad overview of nonlinear optics, followed by a more focused discussion of the beam deflection technique. The material to be investigated, TiN, is introduced. Finally, previous nonlinear optical measurements of TiN thin films are presented.

2.2 Nonlinear Optics

2.2.1 Linear Refraction and Absorption

The index of refraction (n) is the material property which determines how light bends when incident on the material. The index of refraction is unitless, the square root of the ratio of the permittivity of the material to the permittivity of free space. The index of refraction is the ratio of the velocity of light in a vacuum to the velocity of light in the material. Both relationships are shown in Equation 2.1.

$$n = \sqrt{\frac{\epsilon}{\epsilon_0}} = \frac{c}{v} \tag{2.1}$$

where

n = index of refraction

ϵ = permittivity

ϵ_0 = permittivity of free space

c = velocity of light in a vacuum

v = velocity of light in the material

Because light changes speed when moving between materials, two material's in-

dices of refraction describe how light turns between the materials. The relationship between the angles (A and B) and the indices of refraction, known as Snell's Law, is shown in Figure 2.1 and Equation 2.2.

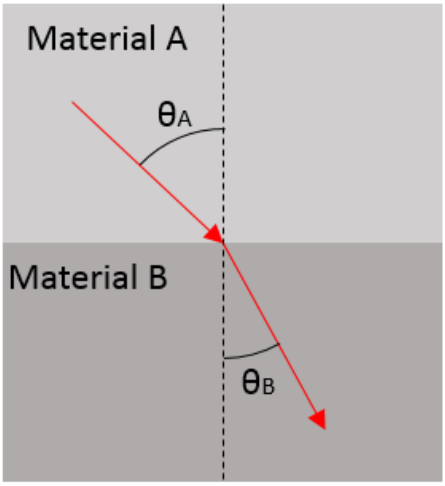

Figure 2.1. Illustration of Snell's Law: Light bends as it travels from one material to another

$$\frac{n_B}{n_A} = \frac{sin(\theta_A)}{sin(\theta_B)} \tag{2.2}$$

where

n_A = index of refraction of material A

n_B = index of refraction of material B

θ_A = angle between the normal of material A and the light

θ_B = angle between the normal of material B and the light

In linear optics, the index of refraction is a function of wavelength, but not a function of the intensity of the incident light. In other words, for a given wavelength, n is constant.

The absorption coefficient (α) is the material property which determines how much incident light is absorbed by the material. The intensity of light transmitted through length z of the material is given by Equation 2.3. The units of the absorption

coefficient are $\frac{1}{\text{Unit Lenght}}$. Like the index of refraction, the absorption coefficient is dependent on wavelength.

$$I(z) = I_0 e^{-\alpha z} \tag{2.3}$$

where

I = light intensity or power per unit area $[W/m^2]$

I_0 = intensity of light incident on the material or I(z=0) $[W/m^2]$

z = distance into material $[m]$

α = absorption coefficient $[1/m]$

2.2.2 Nonlinear Refraction and Absorption

The linear understanding of optics is adequate when describing the behavior of light from the sun, light bulbs or LEDs. However, light from lasers is orders of magnitude more intense. In fact, the electric field $\mathcal{E}$ of light from a laser is 10^5 to 10^8 V/m, similar to interatomic electric fields.[9]

For such intense light, the equations in Section 2.2.1 are insufficient, and higher order terms are needed. The index of refraction is no longer constant, as seen in Equation 2.4.[10]

$$n = n_0 + n_2 I \tag{2.4}$$

where

I = light intensity, or power per unit area $[W/m^2]$

n = index of refraction

n_0 = linear index of refraction

n_2 = nonlinear index of refraction $[m^2/W]$

Absorption is not only a function of intensity, but also of the square of the intensity, as seen in Equation 2.5.

$$\frac{\partial I}{\partial z} = -\alpha I - \alpha_2 I^2 \tag{2.5}$$

where

$I =$ light intensity $[W/m^2]$

$z =$ distance into material $[m]$

$\alpha =$ linear absorption coefficient $[1/m]$

$\alpha_2 =$ nonlinear absorption coefficient $[m/W]$

Measured values of nonlinear absorption and refraction of a selection of materials are listed in Table 2.1.

Material	n_2 10^{15} (cm^2/W)		α_2 (cm/GW)
	1064 nm	532 nm	532 nm
LiF	0.081	0.061	~ 0
MgF_2	0.057	0.057	~ 0
BaF_2	0.14	0.21	~ 0
$NaCl$	1.8		
SiO_2	0.21	0.22	~ 0
MgO	0.39		
Al_2O_3	0.31	0.33	~ 0
BBO	0.29	0.55	~ 0
KBr	0.79	1.27	~ 0
$CaCO_3$	0.29	0.29	
$LiNbO_3$	0.91	8.3	0.38
KTP	2.4	2.3	0.1
ZnS	6.3		3.4
$TeGlass$	1.7	9	0.62
$ZnSe$	29	-68	5.8
$ZnTe$	120		4.2
$CdTe$	-300		22
$GaAs$	-330		26
$RNglass$	2.2		

Table 2.1. NLO properties of selected materials. Adapted from Christodoulides. [3]

2.2.3 Nonlinear mechanisms

The thin film transition metal nitrides are expected to behave either as metals, semiconductors, or a combination of the two. As such, the mechanisms and behavior of metals and semiconductors will be discussed in this section.

2.2.3.1 Nonlinear mechanisms in metals

Metals have relatively strong nonlinear optical properties, which mostly arise from three mechanisms: bound electrons, free electrons and hot electrons.

Bound electron transitions occur at frequencies greater than the band gap. Electrons transfer from the full d-band to the partially filled sp-bands. [7]

Free electron transitions occur at lower frequencies. The absorption band is broadened, and the higher electron temperature contributes to more electron scattering.[7]

The greatest contribution is from the hot electron mechanism. A small amount of the excited electrons are heated to a very high temperature. [7] One model for how these hot electrons dissipate energy is called the "two temperature model". The two temperatures are the temperature of the electron and the temperature of the lattice (or phonon). When heated by an ultrafast laser, the electrons can be much hotter than the lattice for picoseconds. This energy is dissipated in two ways: through electron-electron collisions and electron-phonon collisions. The collision times will be similar, but energy will be transfered more quickly between the less massive electrons. [11]

On a timescale of hundreds of femtoseconds, very hot (order of magnitude thousands K) electrons transfer thermal energy to surrounding electrons. On a timescale of 0.5-4.0 picoseconds, these hot electrons transfer thermal energy to the lattice. On the timescale of several picoseconds, the thermal energy transfers from the electrons to the lattice through electron-phonon coupling. The material will heat up, but as

the electrons and the lattice reach thermal equilibrium, the nonlinear optical response decays. [7]

There have been multiple numerical and experimental explorations of the two temperature model.

Jiang and Tsai implemented full-run quantum treatments to expand the phenomenological two temperature model, and compared calculations to experimental results of gold thin films. For a 200 nm gold film, this model predicts that the electrons and lattice will be at equilibrium in 10 picoseconds for intensity 0.05 J/cm^2, and 15 picoseconds for intensity 0.2 J/cm^2.[11]

Chen, Tzou and Beraun developed a semiclassical model as an alternative to the phenomenological model. The semiclassical model accounts for electron drifting, which phenomenological models do not. The model uses conservation of electron number density, momentum and energy to calculate the transient temperatures of the hot electrons and the lattice. The results of this model applied to 1.0 μm thick gold film are shown in Figure 2.2.The hot electrons both heat and relax more quickly than lattice. The data is presented in picoseconds, but the focus is on the rise of both temperatures, and not the eventual decay. The relaxation time of both the temperature of the hot electrons, T_e, and the lattice, T_l is longer than 16 picoseconds.[2]

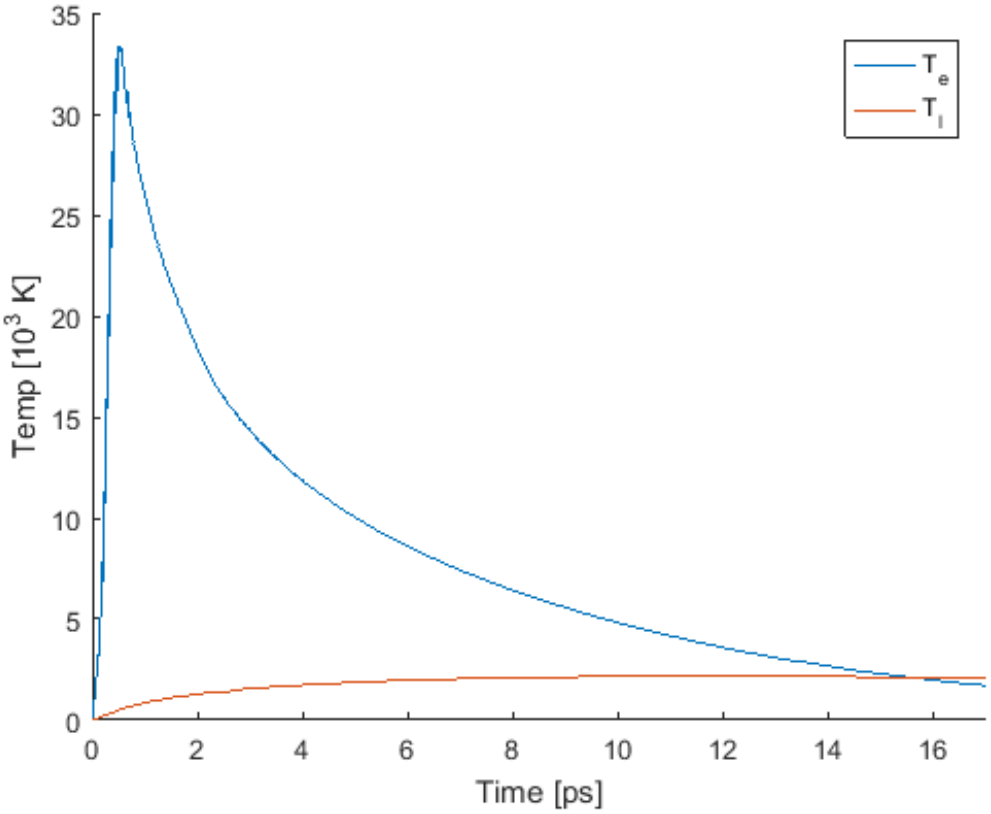

Figure 2.2. Temperatures of hot electrons, T_e, and lattice, T_l at the front surface of a 1.0 μm thick gold film over time. Adapted from Chen. [2]

Bonn, Denzler, Funk and Wolf implemented a similar experimental setup to the beam deflection technique. Like the beam deflection technique, a strong pump beam is used to incite the nonequilibrium state. The weaker probe beam measures changes in reflectivity, and the two beams are offset in time by a mechanical delay. The experiment found that the competing electron-phonon and hot-electron effects well explained the results shape, if not magnitude. [12]

2.2.3.2 Nonlinear mechanisms in semiconductors

There are three dominant nonlinear mechanisms, characteristic of semiconductors: two photon absorption, electron density in conduction band and carrier heating.

The two photon absorption is similar to that discussed in Section 2.2.3.1, but will look slightly different due to the shape of a semiconductor band gap. This version of two photon absorption is shown in Figure 2.3. The effect will last only on the order of femtoseconds.

Carrier heating is analogous to the hot electrons discussed in Section 2.2.3.1, and relaxes on a time scale of picoseconds. [3]

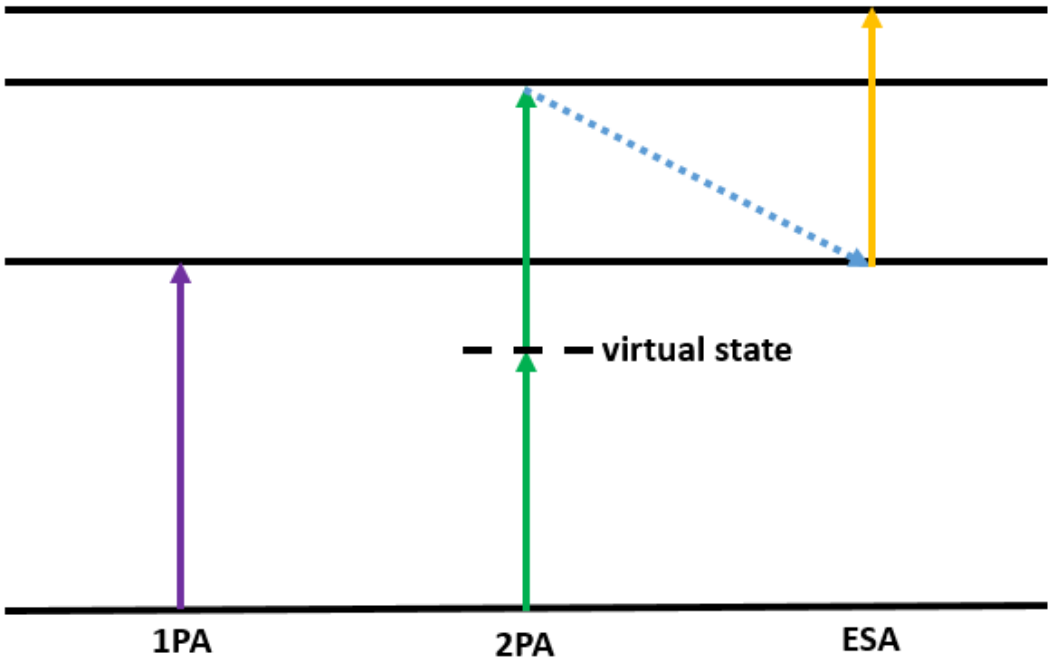

Figure 2.3. One photon absorption is the absorption of a single photon, which excites the molecule to a higher energy electronic state. Two photon absorption is the simultaneous absorption of two photons, which excites the molecule to a higher energy electronic state. Excited state absorption is the absorption of a photon from an already excited state to an even higher energy electronic state. Adapted from Christodoulides. [3]

The number of photons in the conduction band is increased by the absorption of sufficiently energetic incident light, which results in a larger band gap. As illustrated in figure 2.4, the band gap pre-absorption is the difference between the valance and conduction bands. Post-absorption, the band gap is the difference between the now decreased valance band and now increased conduction band. This process is induced near-instantaneously and has a decay time of nanoseconds. [3]

A semiconductor at 0 K will have all the electrons in the valance band, and none in the conduction band. However, all the samples in this work will begin at room temperature. At finite temperatures, some electrons will be in the conduction band. This nuance is left out of the illustration for simplicity.

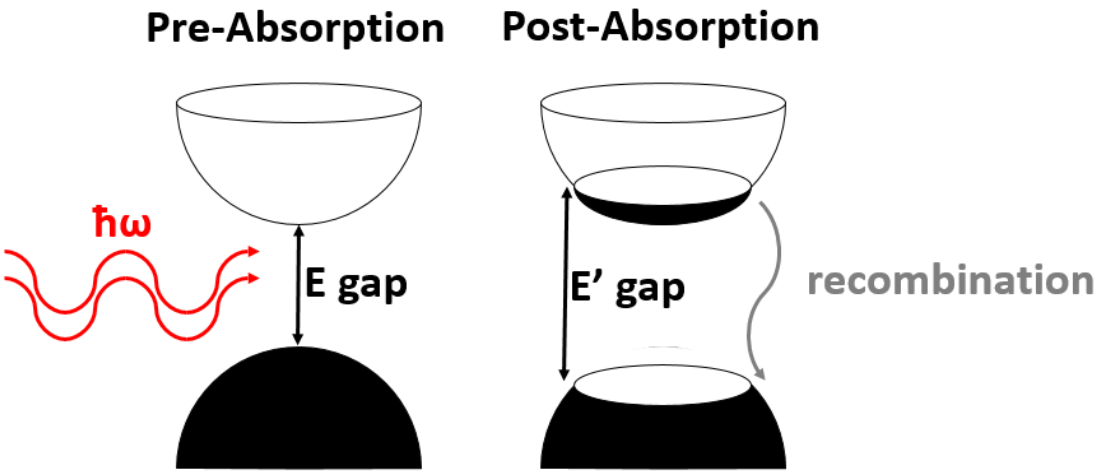

Figure 2.4. Illustration of light incident on a semiconductor. Electron density in the conduction band and band gap size both increase. On the left, pre-absorption, light (red) is incident on a a semiconductor. The valance band is back, representing being filled with electrons. The conduction band is white, representing a lack of electrons. On the right, post-absorption, the gap between the highest unoccupied state in the valance band and the lowest unoccupied state in the conduction band represents the new, larger, band gap. Finally, recombination is shown in gray. Adapted from Christodoulides.[3]

Figure 2.5 shows how these three mechanisms combine. The total response, shown in black, is what would be measured by the beam deflection technique. However, once this shape is recognized, the shape and magnitude of the individual mechanisms can

be intuited.

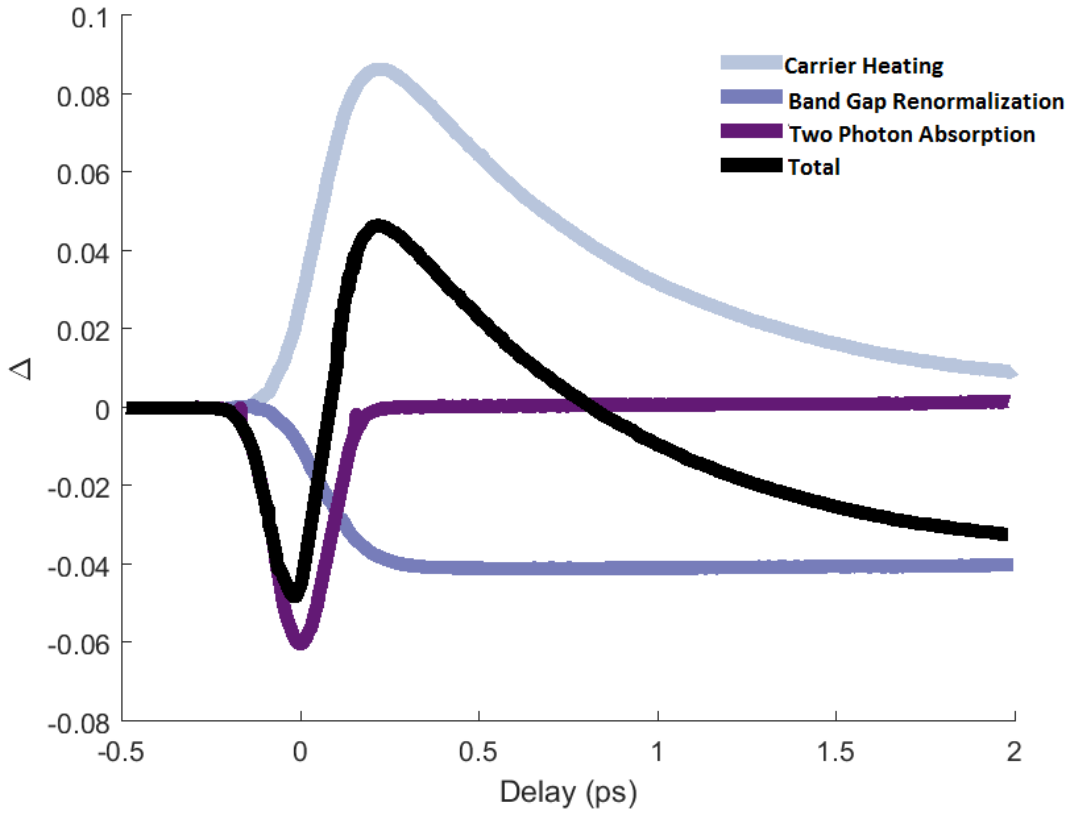

Figure 2.5. The three largest nonlinear mechanisms representative of a semiconductor, and their total effect. The effect of carrier heating is shown in light purple. The effect of number of electrons in the conduction band is shown in medium purple. The effect of Two Photon Absorption is shown in dark purple. These effects add to the total effect, shown in black. Adapted from Christodoulides. [3]

2.3 Measuring NLO Properties

Nonlinear optical properties can be measured by z-scan or beam deflection. The beam deflection technique has the added benefit of providing temporal information.

The z-scan technique uses a single beam. The beam is focused, and the sample is translated through the waist. By moving the sample in the direction of the beam, the area of the beam is changed, while the power is not. This results in a change in intensity, which results in changes to the material's properties, which are measurable by the same beam.

An enhanced variant of this technique is the dual arm z-scan. In this case, the two beams are correlated, so that their noise will be similar. One beam is performs a z-scan on the material of interest, either a solvent or thin film. The other beam performs a z-scan on the solution or substrate. By subtracting the second signal from the first, the effect from the material of interest is isolated.

The beam deflection technique also uses two beams, but in an excite-probe arrangement. A strong pump beam causes a change in material properties, while a weaker probe beam measures the effects. By using ultrafast puled beams, and moving the beams in time, transient nonlinear properties can be measured.

A quad cell detector will be used that measures Total signal, Right-Left signal and Top-Bottom signal. The Total signal will be used to measure absorption. The (Right-Left signal)/(Total signal) will be used to measure refraction, or $\Delta E/E$. Beyond initial alignment, Top-Bottom signal will not be used.

The probe beam should be focused, with the sample directly in the beam waste. The detector should be aligned so that, absent the pump beam, the probe beam is centered. Without the pump beam, as shown in Figure 2.6, only linear absorption and refraction will be present. The total energy collected by the detector will be set to T=1, or 100% transmission, 0% nonlinear absorption. The probe beam is centered on the detector, $\Delta E/E$=0, or no nonlinear refraction.

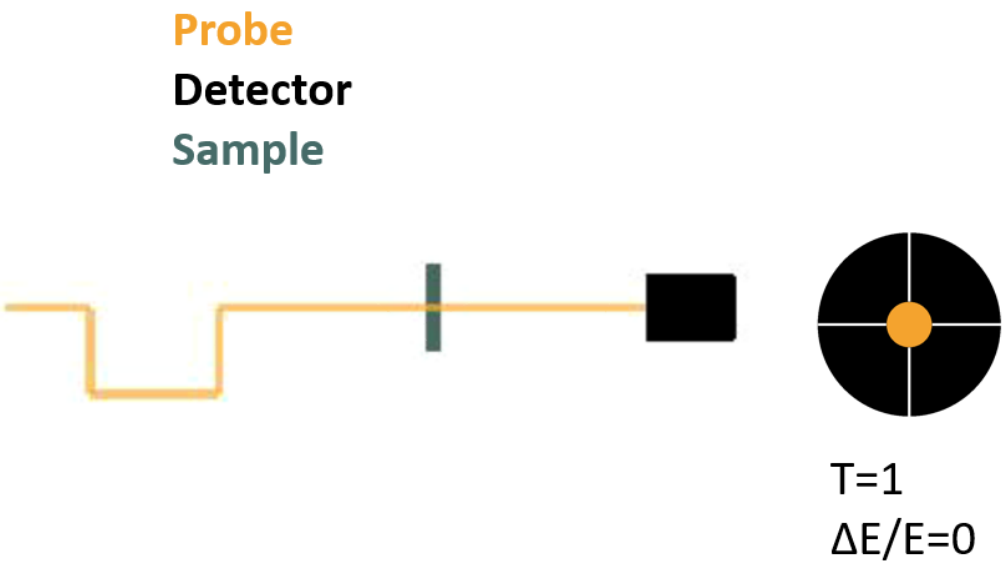

Figure 2.6. Beam deflection technique, only probe. On the left, a schematic of the setup is shown from above. The probe beam (orange) should be parallel to the ground, and centered on the detector (black). The sample (teal) is at the beam's focal point. On the right, the quad cell detector is shown from the front. As discussed, the probe beam is centered. Adapted from Ferdinandus.[4]

The kink in the probe line is a mechanical delay. By moving this delay, the probe pulse can be made to arrive before (negative delay), at the same time (zero delay) or after (positive delay) the pump pulse. This allows for transient data collection.

The pump beam should be angled so as to spatially overlap the probe beam (as shown in Figure 2.7) in the sample, while missing the detector.

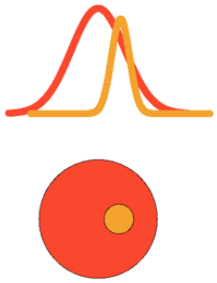

Figure 2.7. The pump beam (red) is larger and stronger. The probe beam (orange) is smaller and weaker. The beams should spatially overlap in the material as shown in this picture.Adapted from Ferdinandus.[4]

Figure 2.8 shows how Figure 2.6 will change by adding this strong pump. Nonlinear absorption cause less total energy of the probe beam to reach the detector, $T < 1$. Nonlinear refraction causes the probe beam to bend, moving it to the side of the detector, $\Delta E/E \neq 0$.[4]

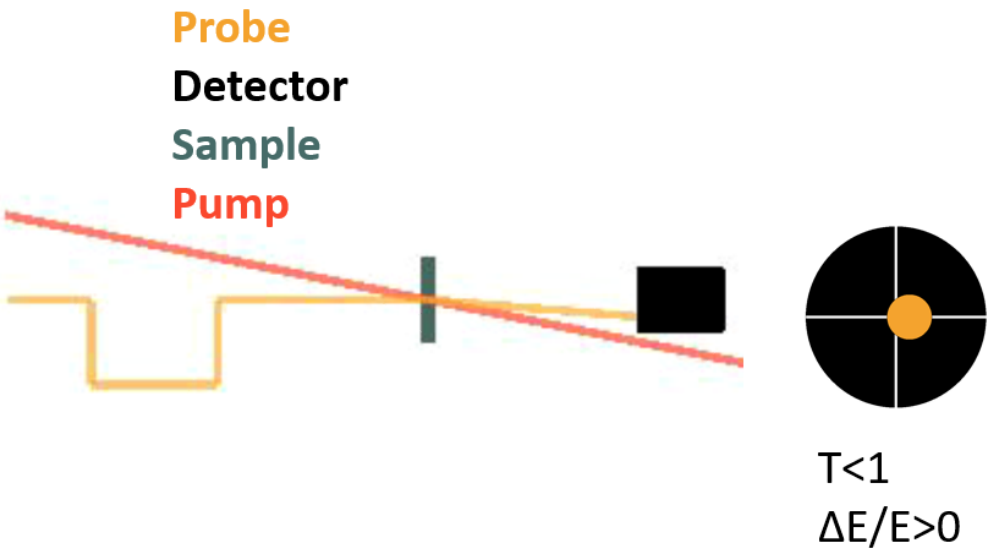

Figure 2.8. Beam deflection technique. On the left, a schematic of the setup is shown from above. The probe beam (orange) and pump beam (red) should be parallel to the ground. The deflection of the probe should be entirely in plane with this schematic. On the right, the quad cell detector is shown from the front. The probe beam has been refracted, and is no longer centered on the detector. Adapted from Ferdinandus.[4]

2.4 Titanium Nitride

TiN is widely used in industry for its desirable properties: excellent high temperature properties, adequate corrosion resistance, and extreme hardness.[13] A summary of these properties is listed in Table 2.2. Section 2.4.1 delves into the chemical reasons for these unique properties. Previous results are presented in Section 2.5.

Property	TiN
Range of Composition	$TiN_{0.6-1.1}$
Color	Golden
Density	5.4 g/cm^2
Melting Point	2950 $°C$
Specific Heat	37.0 $J/molK$
Thermal Conductivity	30 W/mK
Vickers Hardness	21-24 GPa
Modulus of Elasticity	612 GPa
Young's Modulus	590 GPa

Table 2.2. Selected properties of TiN. Adapted from LeClair.[6]

All material properties are sensitive to processing technique, but transition metal nitrides are particularly tunable. Toth discusses major factors which effect material properties. The three factors most relevant to this research are: [13]

- Chemical composition
- Crystal structure and lattice parameters
- Defect structure

This tuneability will be useful in future engineering applications, but presents a challenge to materials characterization. Table 2.1 presents nonlinear properties of selected materials. The materials are specified by their chemical compositions, which may be inadequate to describe the nonlinear properties of a thin film TiN. Films of the same chemical composition, but prepared on different substrates or with a different deposition method, may have different nonlinear properties.

2.4.1 Chemical Composition

It is possible to synthesize nonstoichiometric TiN thin films, and this departure from stoichiometry will change the material properties. This additional dimension of tunability could be useful in the future, but will not be investigated in this work.

Nitrogen has the electron arrangement $1s^2 2s^2 2p^3$. The inner electrons in the first sharp orbital do not bond and are noted as [He] in the box spin diagram, Table 2.3. The outer electrons do effect bonding, and are shown as arrows in the box spin diagram.

N:	[He]	2s	↑↓	2p	↑	↑	↑	

Table 2.3. Box spin diagram of N

Titanium is a transition metal, with electron arrangement $1s^2 2s^2 2p^6 3s^2 3p^6 3d^2 4s^2$. The box spin diagram for Ti is shown in Table 2.4.[14]

Ti:	[Ar]	3d	↑	↑	↑	↑	↑	4s	↑↓	4p			

Table 2.4. Box spin diagram of Ti

Together, Ti and N form titanium nitride, a transition metal nitride. The unique properties of transition metal nitrides are caused by the unique bonding: the hybridized p and d electrons are covalently bonded, and the d electrons are metallicly bonded.[15]

2.4.2 Crystal Structure

Understanding the substrate and thin film crystal structures leads to educated conclusions about how the substrate effects the nonlinear properties of the thin film.

TiN and MgO share the rock salt crystal structure, so called because it is the crystal structure of NaCl. The cubic unit cells are illustrated in Figure 2.9. The size of a cubic unit cell is described by the side of the cube, called the lattice constant, a. The lattice constant of TiN is 4.24 Å. The lattice constant of MgO is 4.21 Å. Al_2O_3 has a trigonal crystal structure, named for the triangular shape. Figure 2.9 shows six of these triangular shaped combined to form a hexagonal unit. THe size of the trigonal cell is described by the side of the triangle, a, and the height of the cell, c. For Al_2O_3, a=4.79 Åand c=12.99 Å. In Figure 2.9, the crystal lattices are to scale, but the atoms are not.

Table 2.5 summarizes the crystal structure of the substrates and the thin film nitrides investigated in this work.

	Crystal Structure	**Lattice Constant**
TiN	Rock Salt	a=4.24 Å
MgO	Rock Salt	a=4.21 Å
Al_2O_3	Trigonal	a=4.79 Å c=12.99 Å

Table 2.5. Crystal structure and size of materials

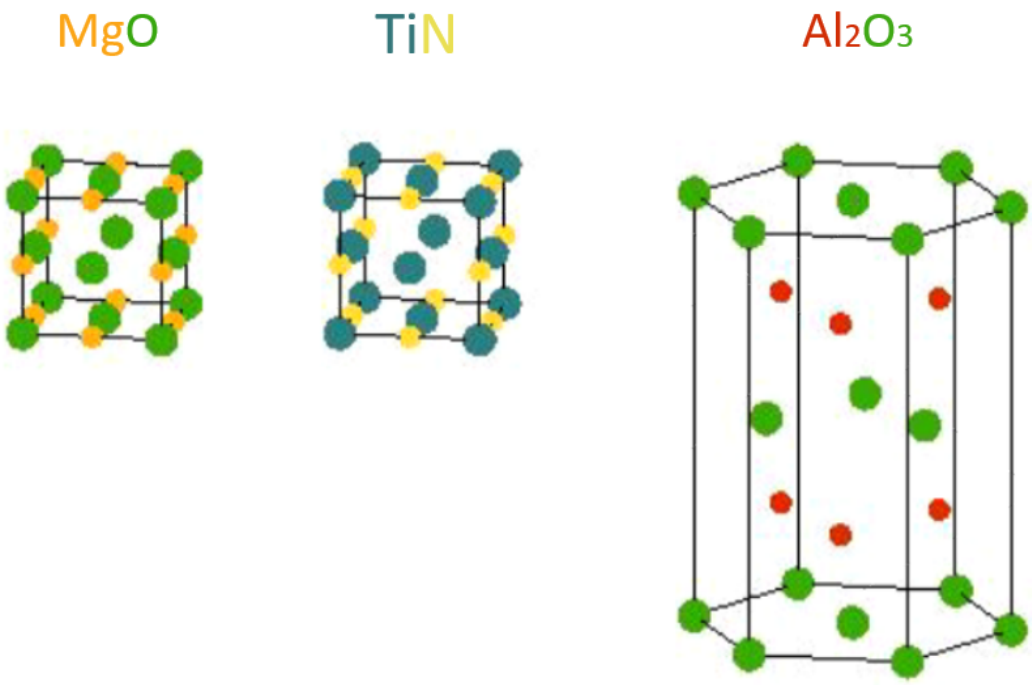

Figure 2.9. Crystals of MgO, TiN, and Al_2O_3. The atoms are not to scale, but the crystals are to scale, relative to each other.

These are the unstrained crystal sizes. The thin film material must stretch or compress to accommodate the substrate. Both MgO and TiN have rock salt structures. The (001) face of TiN grows epitaxially on the (001) face of MgO. Figure 2.10 shows these faces, still to scale. Clearly, the lattice sizes are very similar.

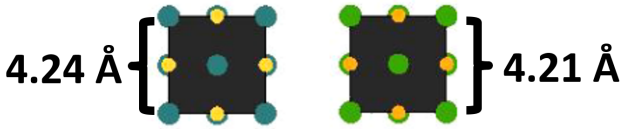

Figure 2.10. The (001) faces of TiN (left) and MgO (right).

Figure 2.11 illustrate how the rock salt crystal is built on the trigonal crystal, which is less intuitive.[16] [17] The TiN is grown on the (0001) face of the Al_2O_3. This face, which is the top of the trigonal shape shown in Figure 2.9, is shown in Figure 2.11. The (111) plane of TiN grows on this face. The (111) face is shown in 2.11 as a triangle. This lattice match is also very close, and allows for epitaxial

growth.

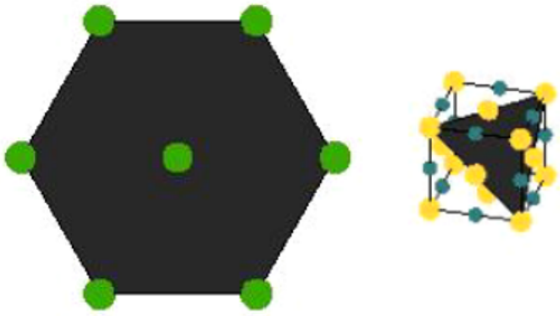

Figure 2.11. The (0001) face of Al_2O_3 (left) and the (111) face of TiN (right).

2.4.3 Defect structure

Even the highest quality thin films will not be perfect crystals, and will have unknown vacancy concentrations and other defects.

Characterizing these defects in nitrides is a "complex problem." Stoichiometric transition metal nitrides will have vacancies at both lattice sites. Stoichiometric TiN has been found to have vacancy concentrations for both Ti and N lattice sites of 4%.[13]

Furthermore, each thin film will actually be made of multiple crystals, introducing grain boundary defects. Since TiN is a closer lattice match to MgO than Al_2O_3, larger crystal sizes are expected on MgO. Grain boundaries will effect NLO properties by inhibiting the transfer of energy through the lattice.

2.5 Previous Work

TiN is a widely researched material, but the researcher know of only two studies of it's nonlinear properties. In 2016, Kinsey et al. measured nonlinear optical properties of thin film TiN with the dual-arm Z-scan technique. The TiN thin films were grown

on fused silica by reactive magnetron sputtering. The TiN was found to exhibit nonlinear absorption and refraction at a similar order of magnitude to metals.[18] In 2016, Reed et al. used the beam deflection technique to measure nonlinear optical properties of thin film TiN grown on fused silica.

The results were an instantaneous nonlinearity and a single long decay. A representative result is plotted in Figure 2.12 The measured n_2, α_2 and τ are listed in Table 2.6. [5]

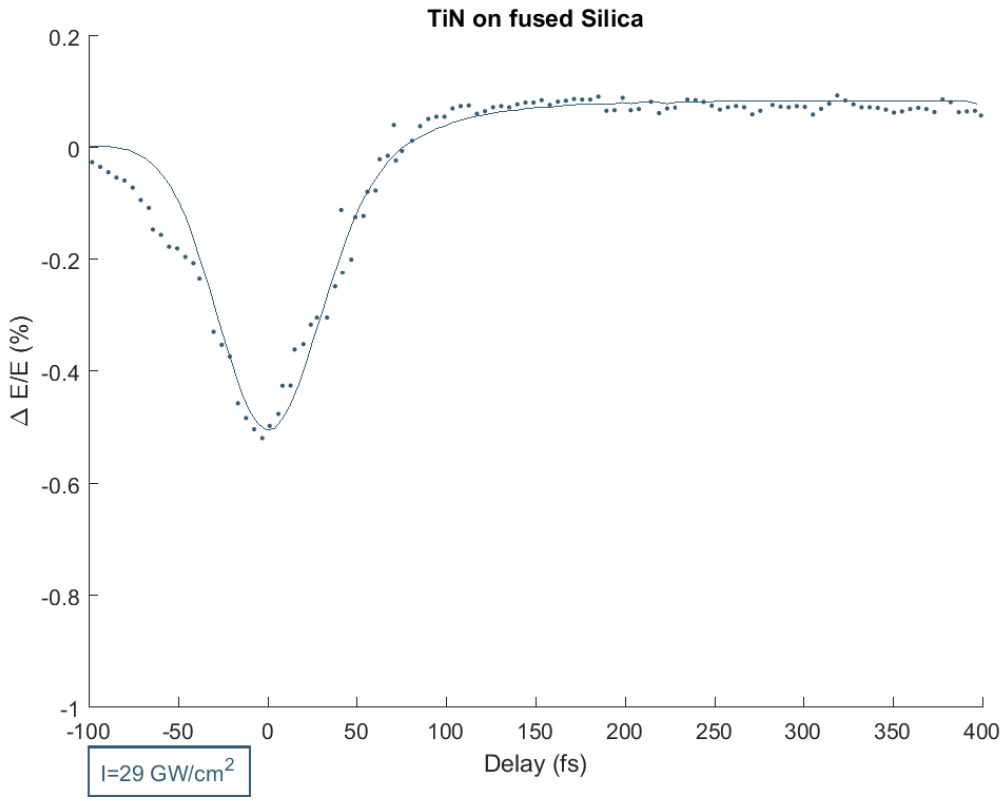

Figure 2.12. Transient nonlinear refraction of thin film TiN on fused silica. Data as points, fit as line. Adapted from Reed. [5]

Table 2.6. NLO properties of thin film TiN on fused silica. Adapted from Reed. [5]

Sample	n_2 electronic ($10^{-15}m2/W$)	n_2 of τ_{rise} ($10^{-19}m^2/W$)	τ_{rise} fs	n_2 of τ_{fall} ($10^{-15}m^2/W$)	τ_{fall} ps
TiN 800 deg C	-0.6	-0.5	40	478	435
TiN 330 deg C	-1.4	-0.5	40	434	435

III. Research Methodology

3.1 Beam Deflection

Beam deflection measurements, described in Section 2.3, are collected for the bare substrate and the covered substrate of each sample.

3.1.1 Probe and Pump Beams

The fundamental beam is produced by a KM Labs Wyvern 1000-10 Ti:sapphire laser, producing 790 nm pulses at 35 fs (FWHM) temporal pulse duration at an energy of 4.2 mJ at a repetition rate of 1 kHz. This fundamental beam is split into the pump and probe beams.

A Traveling-wave Optical Parametric Amplifier (TOPAS) is used to convert the probe beam to 650 nm, 55 fs. Because the TOPAS distorts the beam shape, this beam must be spatially filtered to reattain a Gaussian profile. A roof mirror on on a motorized stage is used to control the delay. Following the roof mirror, a variable attenuator is used to control the intensity of the probe beam. The probe beam's intensity is constant, but this level of control is useful when initially setting up the experiment. An off-axis parabolic mirror is used to focus the probe beam. The sample is placed in the focus of the probe, while the detector is placed past the focus.

A mechanical optical chopper (ThorLabs MC-2000) modulates the pump beam at 286 Hz. This modulation is used by the lock-in amplifier to collect the data. Following the chopper, a variable attenuator is used to control the intensity of the pump beam. Multiple pump intensities are collected for each sample, so having this level of control is vital. As shown in Figure 2.8, the pump beam is aligned so that it overlaps the probe beam in the sample, but misses the detector. A rough estimate of spacial overlap can be found visually. Spacial overlap is improved by finding a signal

in a material with a known long response, with the delay stage at positive delay. This has the added benefit of assuring the spacial overlap has been maximized in the thin film, and not the substrate.

The pump and probe lines are the same length when the delay stage is at zero delay. Depending on experimental set up, one of the lines may need to be lengthened, so that this "zero delay" lies at a reasonable position of the delay stage.

3.1.2 Detector and Lock-in

The quad cell detector (Model) is connected to a lock-in amplifier (MODEL SR830 DSP Lock-In Amplifier). The lock-in amplifier measures both the Total signal, and the Right-Left signal.

3.1.3 Measurements

Data from the lock-in is useless without knowing the intensities of the pump and probe beams at the sample. Knife-edge scans are used to find beam size, while power meters are used to find power.

IV. Results

4.1 Chapter Overview

In order to understand the NLO propertied of the materials, it is necessary to first find the linear optical properties. To this end, X-ray diffraction (XRD), ellipsometry and atomic force microscopy (AFM) measurements were taken for each sample. Details of these measurements can be found in Appendix A, and the resulting linear properties are included in Section 4.2.

For all samples, the thin film partially covers the substrate. A beam deflection measurement is collected for the bare substrate and the film covered substrate. The NLO effects of the film are isolated by subtracting the bare substrate data from the film covered Substrate data.

For all samples, two time scales are investigated. The shorter time scale is 600 fs, and is used to measure the magnitude of the electronic NLO properties, $n_{2,electonic}$ and $\alpha_{2,electonic}$. These measurements are presented in Section 4.3.1.

The longer time scale is 1.5 ns, and is useful for measuring the fall time (τ_{fall}) of long responses. There may be multiple NLO mechanisms in this time scale. If so, they will be numbered with ($\tau_{fall,1}$) being the shortest. These measurements are presented in Section 4.3.2.

Once the number and relative magnitude of long responses has been determined in Section 4.3.2, the short time scale can again be used to find the nonlinear index of refraction ($n_{2,\tau}$) and nonlinear absorption coefficient ($\alpha_{2,\tau}$) for each mechanism. These measurements are presented in Sections 4.3.4 and 4.3.3.

Finally, the NLO properties of each sample are compared in Section 4.3.5.

4.2 Linear

From the ellipsometry data, included in Appendix A, the linear absorption coefficient, α from Equation 2.5, and linear index of refraction, n_0 from Equation 2.4, are found for each sample. These values are included in Table 4.1.

The substrate nor deposition power are expected to strongly effect linear optical propertied. As expected, these values are vary similar.

Table 4.1. Linear absorption coefficient α and linear index of refraction n_0 of each sample

	α[E5 1/cm]	n_0
TiN on MgO, 50 W	1.5	3.89
TiN on Al_2O_3, 50 W	1.8	3.94
TiN on MgO, 100 W	1.9	3.82

4.3 Beam Deflection

4.3.1 Electronic

No thin film TiN samples show an electronic response. Since this result is consistent for all samples, a single sample will be used to illustrate. The short time scale data for TiN on MgO, 50 W Sample is shown in Figure 4.1. Throughout this paper, the $\Delta E/E$ results will be shown in the top half of the figure, and transmission results will be shown in the bottom half of the figure.

The data collected for the bare substrate is plotted in red. The positive peak centered at zero delay is the only feature in the $\Delta E/E$ data. This indicates an electronic response. There are no features in the bare substrate transmission results.

The data collected for the film covered substrate is plotted in black. In the $\Delta E/E$ data, a similar positive peak is followed by a negative tail. In the transmission results, there is a negative tail.

By subtracting the bare substrate results from the film covered substrate results, the the NLO effects of the film are isolated and shown in green. As clearly shown, the electronic response measured in the film covered substrate data is entirely accounted for by the bare substrate. The film contributes no electronic response.

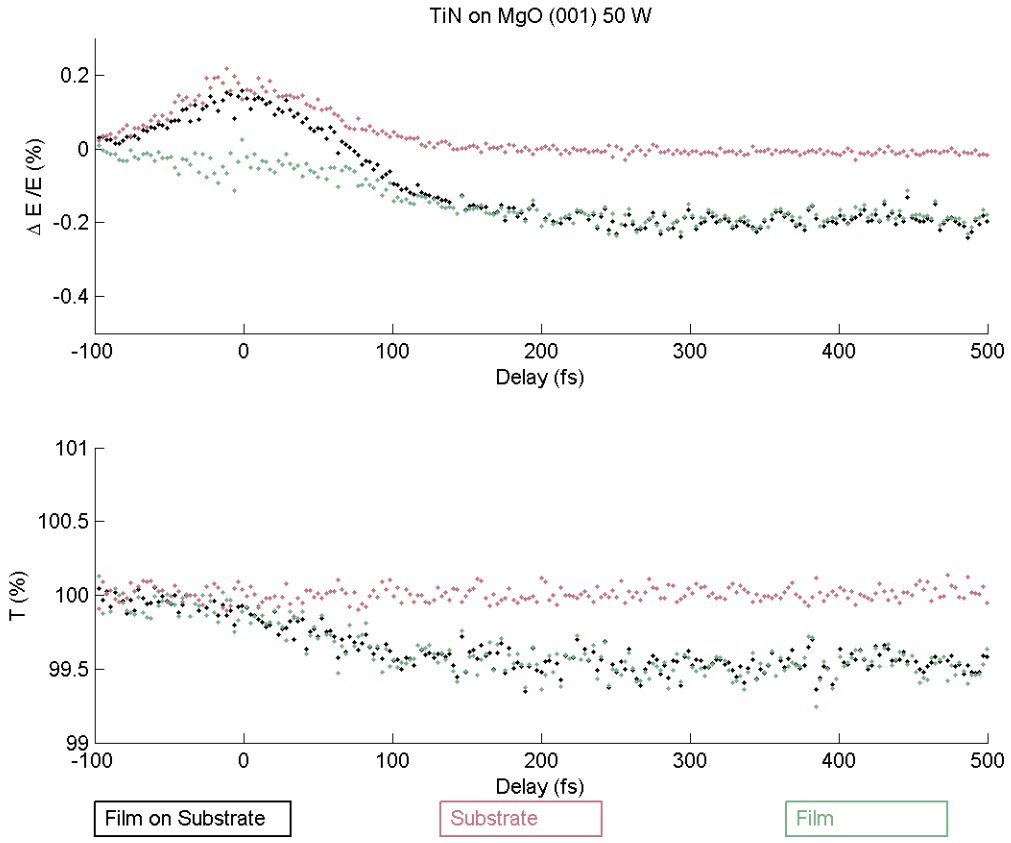

Figure 4.1. Beam Deflection data for TiN on MgO, 50 W: Results are collected for film covered substrate (black) and bare substrate (red). The difference between these is the effect of the film (green).

4.3.2 Long Delay

The results from the 600 fs range shown in Section 4.3.1 indicate the presence of at least one long delay mechanism. The negative tails on the $\Delta E/E$ and transmission results are the rise of these mechanisms. To measure this decay, a similar number of data points are collected, spanning 1.5 ns instead of 600 fs. In fact, this is not

enough time for the mechanisms to entirely decay. As shown in Figures 4.2-4.4, at 1.5 nanoseconds, the $\Delta E/E$ signal is not consistently returned to 0%, and the transmission is not consistently returned to 100%. However, the time span is sufficient to fit models to the data.

If there is a single long delay mechanism, an exponential model, Equation 4.1, will be the best fit for the data. If there are two long delay mechanisms, a biexponential fit, Equation 4.2 will be the best fit for the data.

$$y = Ce^{-t/\tau_{fall}} \tag{4.1}$$

$$y = C_1 e^{-t/\tau_{fall,1}} + C_2 e^{-t/\tau_{fall,2}} \tag{4.2}$$

To determine whether to use a single exponential or biexponential model, coefficient of determination, R^2 is employed.

In the past, such as Reed et al.[5], a single decay has been modeled. This is not physically incorrect, but does conflate electron-electron and electron-phonon coupling. It is possible that the two mechanisms have such similar rise and fall times as to be indistinguishable. In such a case, it would be inappropriate to arbitrarily separate the data into two mechanisms, and the simpler single exponential model is appropriate.

The coefficient of determination measures the proportion of the variance in the data which is predicted by the model. R^2 values show that ranges from 0 (the model explains none of the data) to 1 (the model perfectly explains the data). Since there is noise in the collected data, no R^2 will be equal to 1, but a higher R^2 indicates that the model is explaining more of the variance. If the R^2 of the biexponential model is sufficiently larger than the R^2 of the exponential model, this difference represents the benefit of fitting the more complicated biexponential model.

Figures 4.2, 4.3 and 4.4 show the collected 1.5 ns timescale data in data points. The exponential model is drawn with a dashed line, and the biexponential model is drawn with a dashed line. Visual inspection of the two models, as well as the R^2 values show that the biexponential model is the appropriate fit. There are two long decay mechanisms. As such, $\tau_{fall,1}$ and $\tau_{fall,2}$ from Equation 4.2 will be presented. No time constants for the less appropriate exponential model, Equation 4.1 will be presented.

Figure 4.2 presents the beam deflection results on a 1.5 ns time scale for the TiN on MgO, 50 W sample, along with two possible models. The $\Delta E/E$ exponential fit has an R^2 of .77, while the $\Delta E/E$ biexponential fit has an R^2 of .96. The transmission exponential fit has an R^2 of .81, while the transmission biexponential fit has an R^2 of .95. The biexponential model is the appropriate model for this data. There are two long decay mechanisms. The time constants for the $\Delta E/E$ data are $\tau_{fall,1} = 130$ ps and $\tau_{fall,2} = 2.34$ ns. The time constants for the transmission data are $\tau_{fall,1} = 120$ ps and $\tau_{fall,2} = 1.40$ ns.2

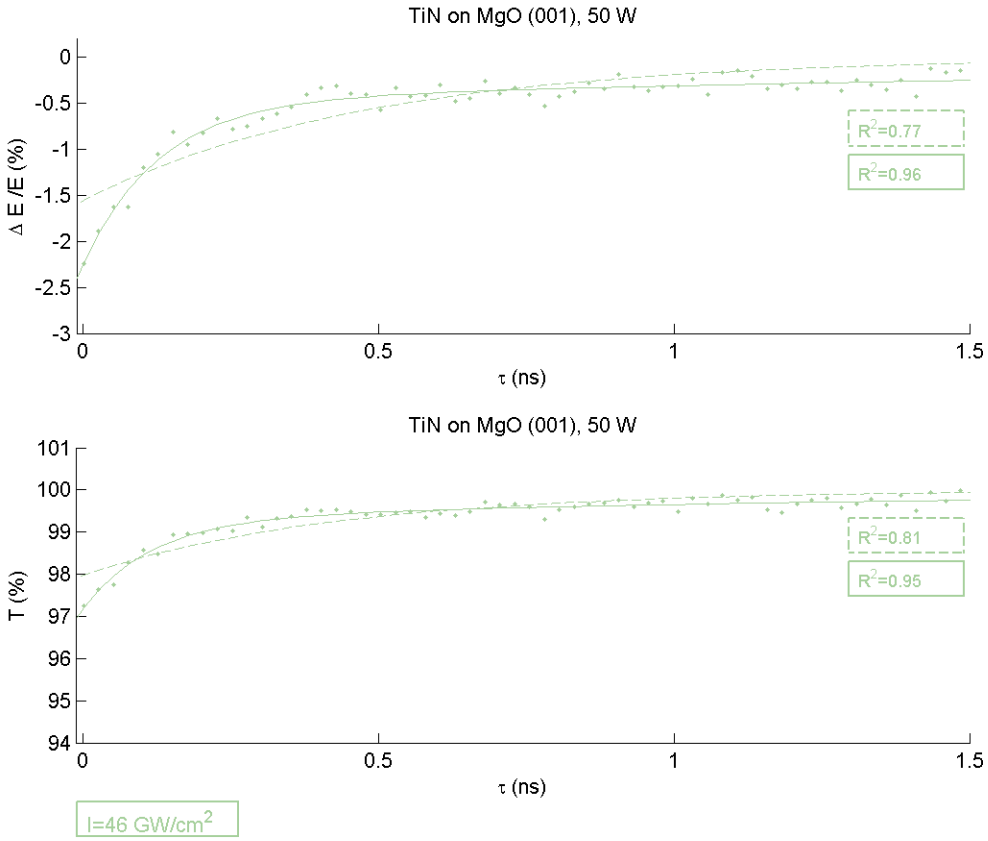

Figure 4.2. Long Delay Data and Fits for TiN on MgO, 50 W

Figure 4.3 presents the beam deflection results on a 1.5 ns time scale for the TiN on Al_2O_3, 50 W sample, along with two possible models. The $\Delta E/E$ exponential fit has an R^2 of .87, while the $\Delta E/E$ biexponential fit has an R^2 of .97. The transmission exponential fit has an R^2 of .83, while the transmission biexponential fit has an R^2 of .97. The biexponential model is the appropriate model for this data. There are two long decay mechanisms. The time constants for the $\Delta E/E$ data are $\tau_{fall,1} = 120$ ps and $\tau_{fall,2} = 2.34$ ns. The time constants for the transmission data are $\tau_{fall,1} = 90$ ps and $\tau_{fall,2} = 1.15$ ns.

2

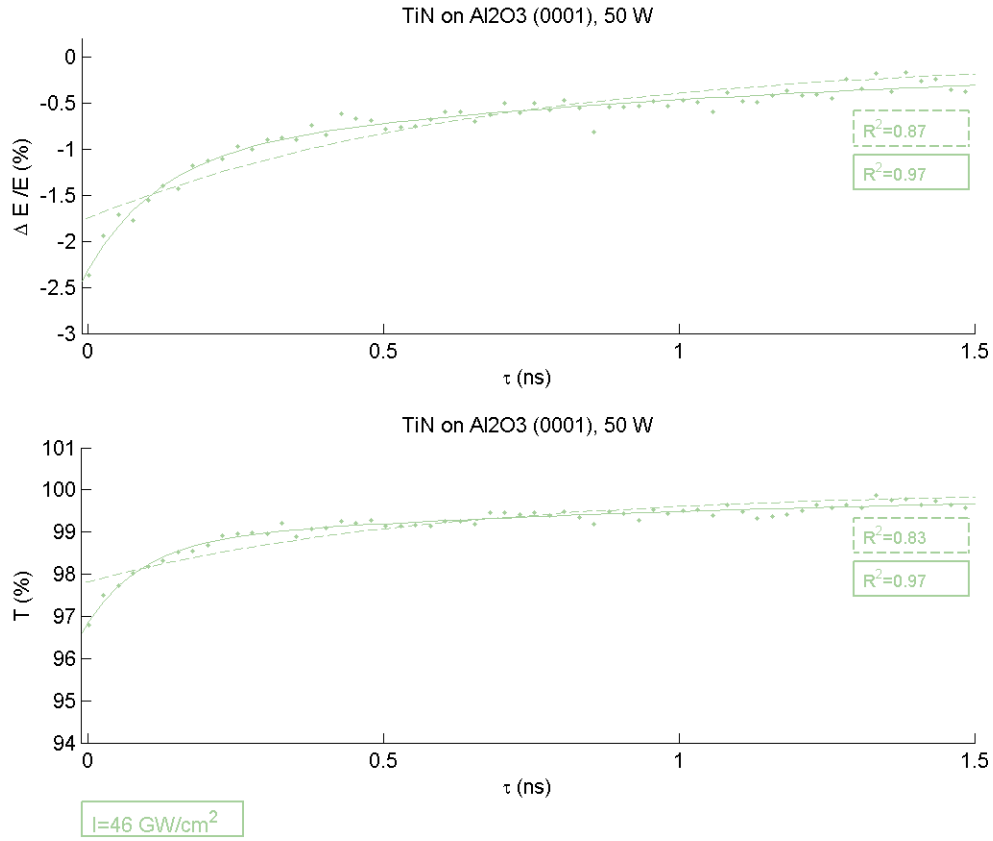

Figure 4.3. Long Delay Data and Fits for TiN on Al_2O_3, 50 W

Figure **??** presents the beam deflection results on a 1.5 ns time scale for the TiN on MgO, 100 W sample, along with two 8possible models. The $\Delta E/E$ exponential fit has an R^2 of .82, while the $\Delta E/E$ biexponential fit has an R^2 of .90. The transmission exponential fit has an R^2 of .85, while the transmission biexponential fit has an R^2 of .92. The biexponential model is the appropriate model for this data. There are two long decay mechanisms. The time constants for the $\Delta E/E$ data are $\tau_{fall,1} = 130$ ps and $\tau_{fall,2} = 1.00$ ns. The time constants for the transmission data are $\tau_{fall,1} = 80$ ps and $\tau_{fall,2} = 0.71$ ns.

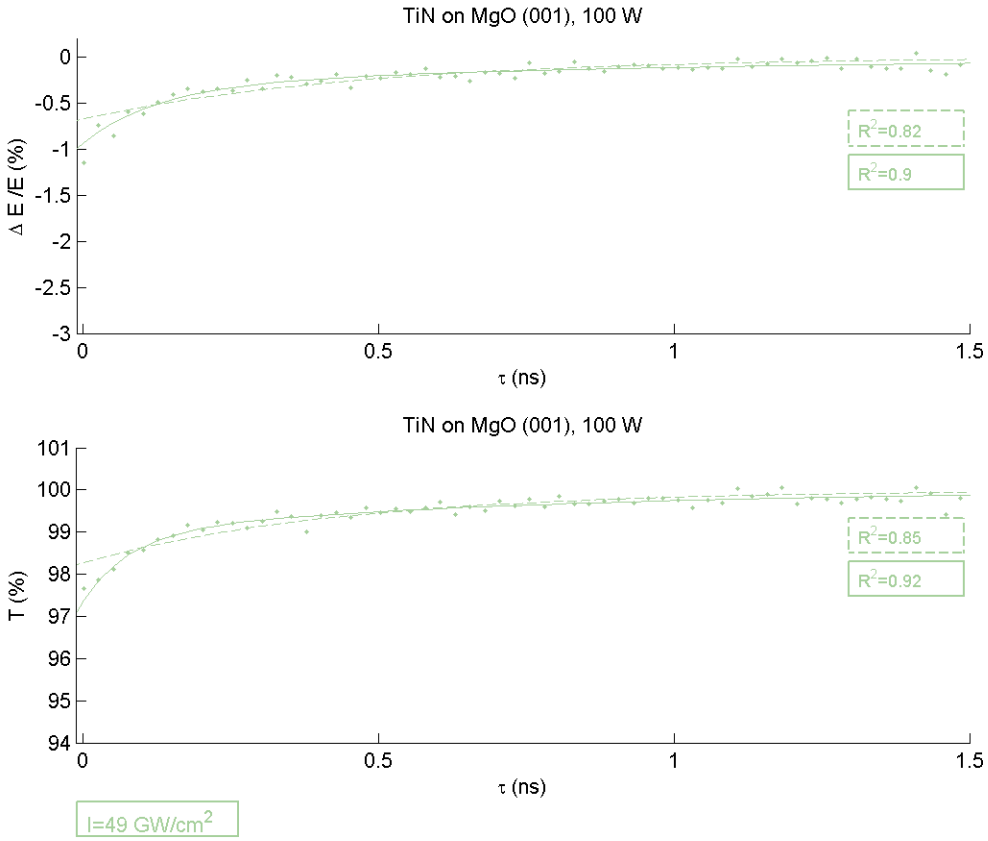

Figure 4.4. Long Delay Data and Fits for TiN on MgO, 100 W

Figure 4.5 presents the $\tau_{fall,1}$ for each sample, found in Section 4.3.2. The time constants are indicated with light blue dots. Also included in the figure are the 95% confidence intervals around the time constants, shown with light blue lines. All time

constants are on the order of magnitude of 100 picoseconds. Based on this conclusion, further calculations and fits will use $\tau_{fall,1} = 97ps$.

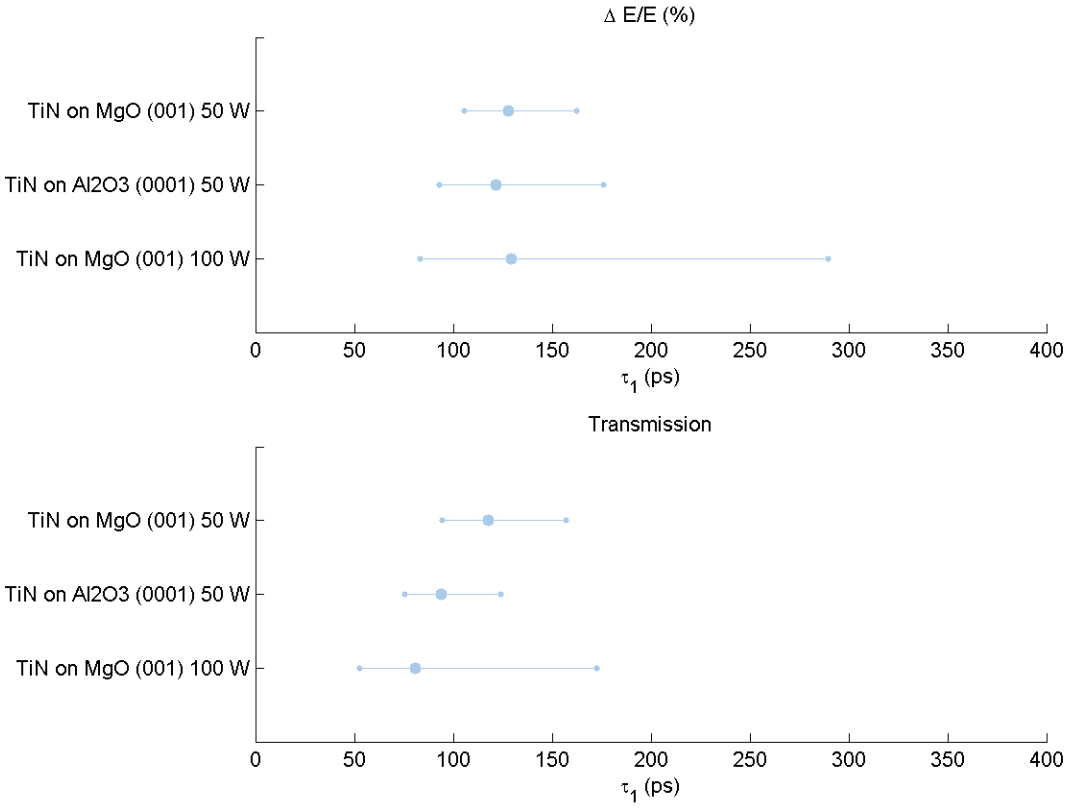

Figure 4.5. $\tau_{fall,1}$ **for each sample, with 95% Confidence Intervals**

Comparing the TiN on MgO, 50 W (top) to the TiN on Al_2O_3, 50 W (middle), contributes to objective 2. The NLO property $\tau_{fall,1}$ is not significantly altered by changing the substrate from MgO to Al_2O_3.

Comparing the TiN on MgO, 50 W (top) to the TiN on MgO, 100 W (bottom), contributes to objective 3. The NLO property $\tau_{fall,1}$ is not significantly altered by changing the deposition power from 50 W to 100 W.

Figure 4.6 presents the $\tau_{fall,2}$ for each sample, found in Section 4.3.2. The time constants are indicated with dark blue dots. Also included in the figure are the 95% confidence intervals around the time constants, shown with dark blue lines. All time

constants are on the order of magnitude of nanoseconds. Based on this conclusion, further calculations and fits will use $\tau_{fall,2} = 1.1ns$.

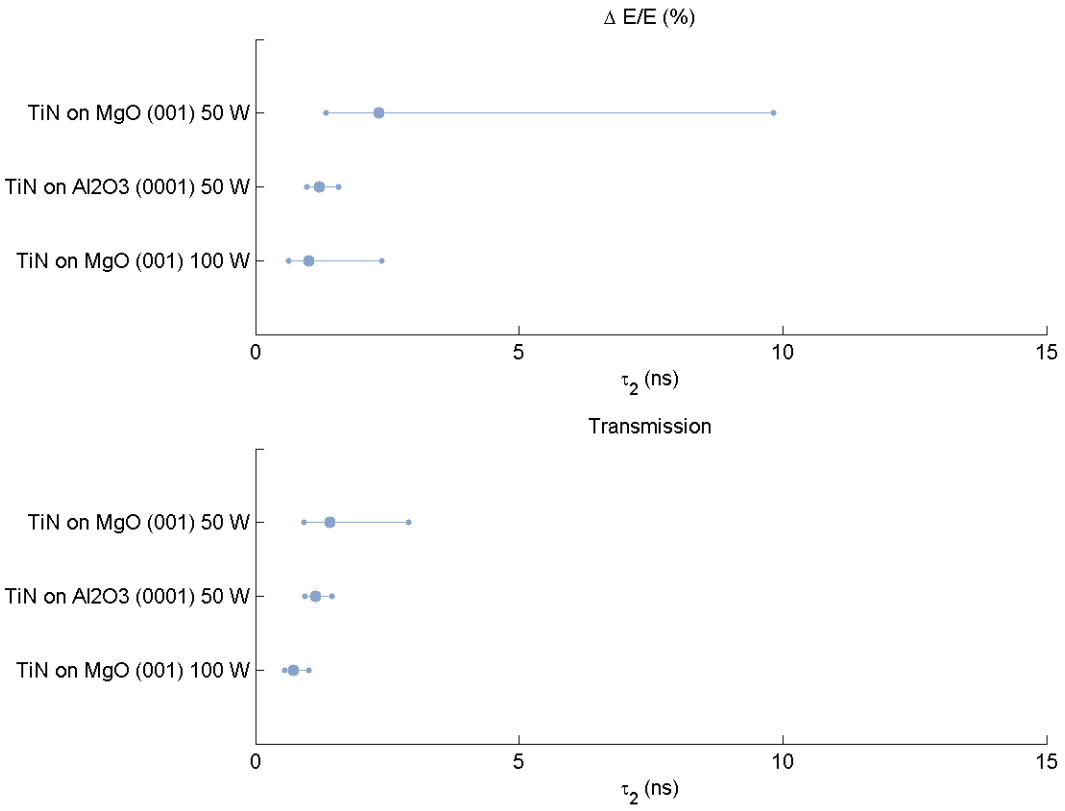

Figure 4.6. $\tau_{fall,2}$ **for each sample, with 95% Confidence Intervals**

Comparing the TiN on MgO, 50 W (top) to the TiN on Al_2O_3, 50 W (middle), contributes to objective 2. The NLO property $\tau_{fall,2}$ is not significantly altered by changing the substrate from MgO to Al_2O_3.

Comparing the TiN on MgO, 50 W (top) to the TiN on MgO, 100 W (bottom), contributes to objective 3. The NLO property $\tau_{fall,2}$ is not significantly altered by changing the deposition power from 50 W to 100 W.

4.3.3 NLO Properties of Picosecond Long Decay

In Section 4.3.1 it was concluded that the TiN films have no electronic response. In Section 4.3.2 it was concluded that the TiN films have two long delay mechanisms. Putting this information together, the 600 fs time scale beam deflection data shows the rise of the two long delay mechanisms. In this section, the data will be fit with $\tau_2 = 1.1ns$, finding n_{2,τ_2}, and α_{2,τ_2}. In Section 4.3.4, the data will be fit with $\tau_2 = 97ps$, finding n_{2,τ_2}, and α_{2,τ_2}.

Beam deflection measurements are collected at multiple pump intensities. The NLO properties, n_2 and α_2, are independent of pump intensity. Multiple intensities act as multiple trials and agreement demonstrates repeatability. The fit for each intensity is completed separately and results are averaged to find final values.

Figures 4.7 and 4.8 present the beam deflection results on the 600 fs time scale for the TiN on MgO, 50 W thin film.

The data points in Figure 4.7 show the collected data of $\Delta E/E$ and transmission data for the TiN on MgO, 50 W sample, for pump intensity $I = 44GW/cm^2$. The solid line in Figure 4.7 shows the expected values of $\Delta E/E$ and transmission when the nonlinear index of refraction $n_{2,\tau_1} = -6.0$ [E-14 m^2/W] and the nonlinear absorption coefficient $\alpha_{2,\tau_1} = 3.5$ [E-7 m/W]. Figure 4.7 shows that these values accurately model the collected data. The noise in the data from Figure 4.7 indicates an uncertainty of $n_{2,\tau_1} \pm 1.0$ [E-14 m^2/W] and $\alpha_{2,\tau_1} \pm 1.5$ [E-7 m/W].

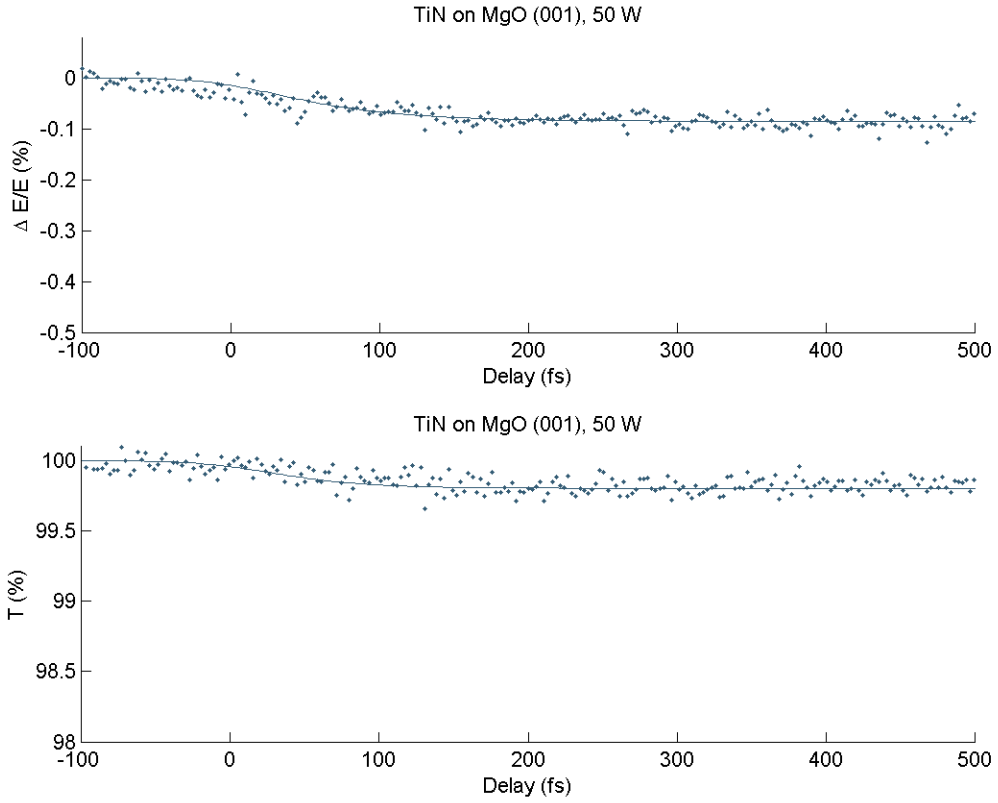

Figure 4.7. Short Delay Data and Fits for TiN on MgO, 50 W, $\tau_1 = 97ps$, $I = 44GW/cm^2$

The data points in Figure 4.8 show the collected data of $\Delta E/E$ and transmission data for the TiN on MgO, 50 W sample, for pump intensity $I = 69GW/cm^2$. The solid line in Figure 4.8 shows the expected values of $\Delta E/E$ and transmission when the nonlinear index of refraction $n_{2,\tau_1} = -5.6$ [E-14 m^2/W] and the nonlinear absorption coefficient $\alpha_{2,\tau_1} = 3.8$ [E-7 m/W]. Figure 4.8 shows that these values accurately model the collected data. The noise in the data from Figure 4.8 indicates an uncertainty of $n_{2,\tau_1} \pm 1.1$ [E-14 m^2/W] and $\alpha_{2,\tau_1} \pm 1.2$ [E-7 m/W].

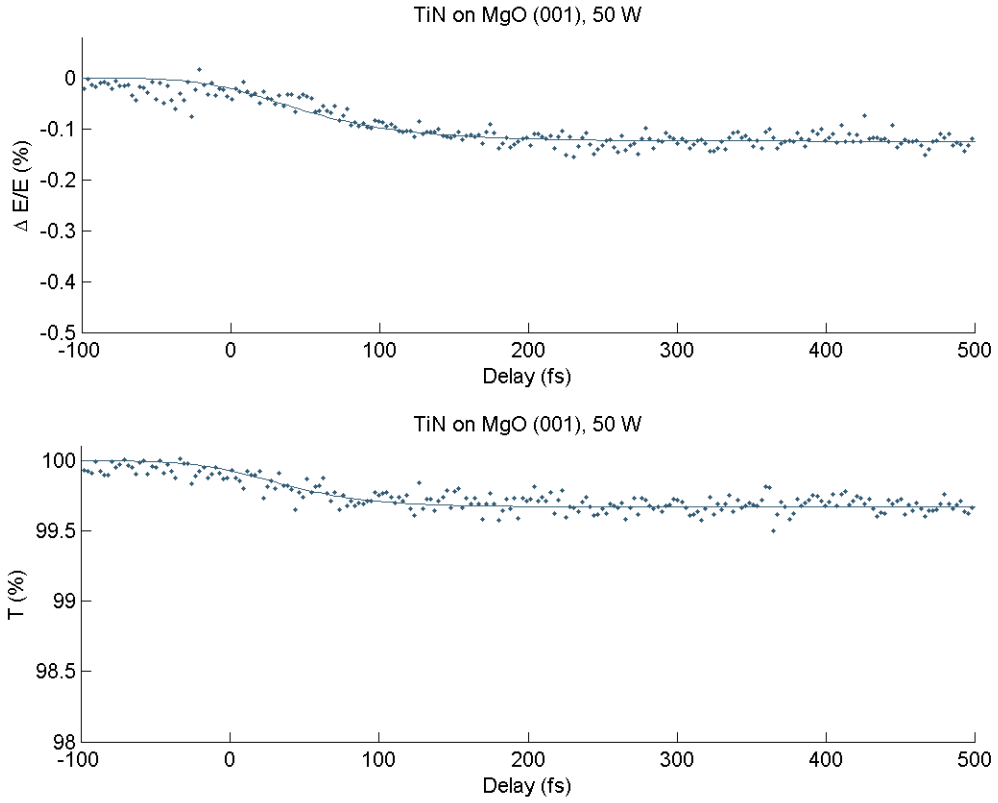

Figure 4.8. Short Delay Data and Fits for TiN on MgO, 50 W, $\tau_1 = 97ps$, $I = 69GW/cm^2$

Figures 4.9 and 4.10 present the beam deflection results on the 600 fs time scale for the TiN on Al_2O_3, 50 W thin film.

The data points in Figure 4.9 show the collected data of $\Delta E/E$ and transmission data for the TiN on Al_2O_3, 50 W sample, for pump intensity $I = 44GW/cm^2$. The solid line in Figure 4.9 shows the expected values of $\Delta E/E$ and transmission when the nonlinear index of refraction $n_{2,\tau_1} = -8.5$ [E-14 m^2/W] and the nonlinear absorption coefficient $\alpha_{2,\tau_1} = 4.5$ [E-7 m/W]. Figure 4.9 shows that these values accurately model the collected data. The noise in the data from Figure 4.9 indicates an uncertainty of $n_{2,\tau_1} \pm 1.5$ [E-14 m^2/W] and $\alpha_{2,\tau_1} \pm 1.5$ [E-7 m/W].

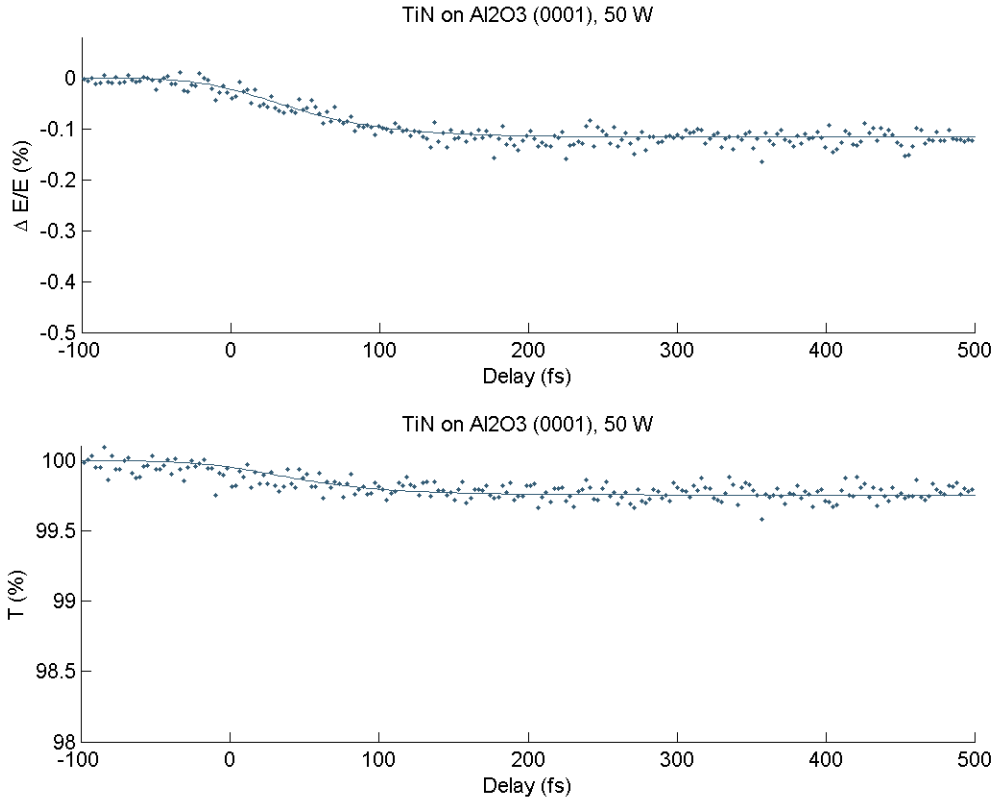

Figure 4.9. Short Delay Data and Fits for TiN on Al_2O_3, 50 W, $\tau_1 = 97ps$, $I = 44GW/cm^2$

The data points in Figure 4.10 show the collected data of $\Delta E/E$ and transmission data for the TiN on Al_2O_3, 50 W sample, for pump intensity $I = 69GW/cm^2$. The solid line in Figure 4.10 shows the expected values of $\Delta E/E$ and transmission when the nonlinear index of refraction $n_{2,\tau_1} = -9.0$ [E-14 m^2/W] and the nonlinear absorption coefficient $\alpha_{2,\tau_1} = 4.5$ [E-7 m/W]. Figure 4.10 shows that these values accurately model the collected data. The noise in the data from Figure 4.10 indicates an uncertainty of $n_{2,\tau_1} \pm 2.0$ [E-14 m^2/W] and $\alpha_{2,\tau_1} \pm 1.5$ [E-7 m/W].

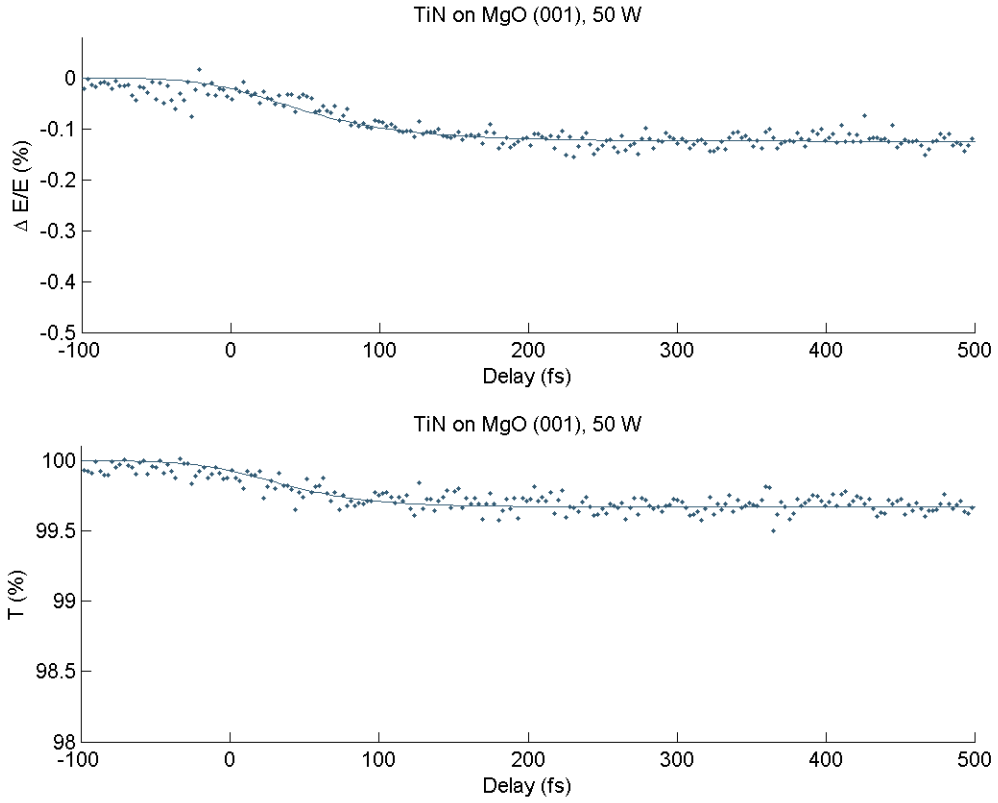

Figure 4.10. Short Delay Data and Fits for TiN on MgO, 50 W, $\tau_1 = 97ps$, $I = 69GW/cm^2$

Figures 4.11,4.12 and 4.13 present the beam deflection results on the 600 fs time scale for the TiN on Mgo, 100 W thin film.

The data points in Figure 4.11 show the collected data of $\Delta E/E$ and transmission data for the TiN on MgO, 100 W sample, for pump intensity $I = 36GW/cm^2$. The solid line in Figure 4.11 shows the expected values of $\Delta E/E$ and transmission when the nonlinear index of refraction $n_{2,\tau_2} = -20$ [E-14 m^2/W] and the nonlinear absorption coefficient $\alpha_{2,\tau_2} = 9.5$ [E-7 m/W]. Figure 4.11 shows that these values accurately model the collected data. The noise in the data from Figure 4.11 indicates an uncertainty of $n_{2,\tau_2} \pm 4$ [E-14 m^2/W] and $\alpha_{2,\tau_2} \pm 3.5$ [E-7 m/W].

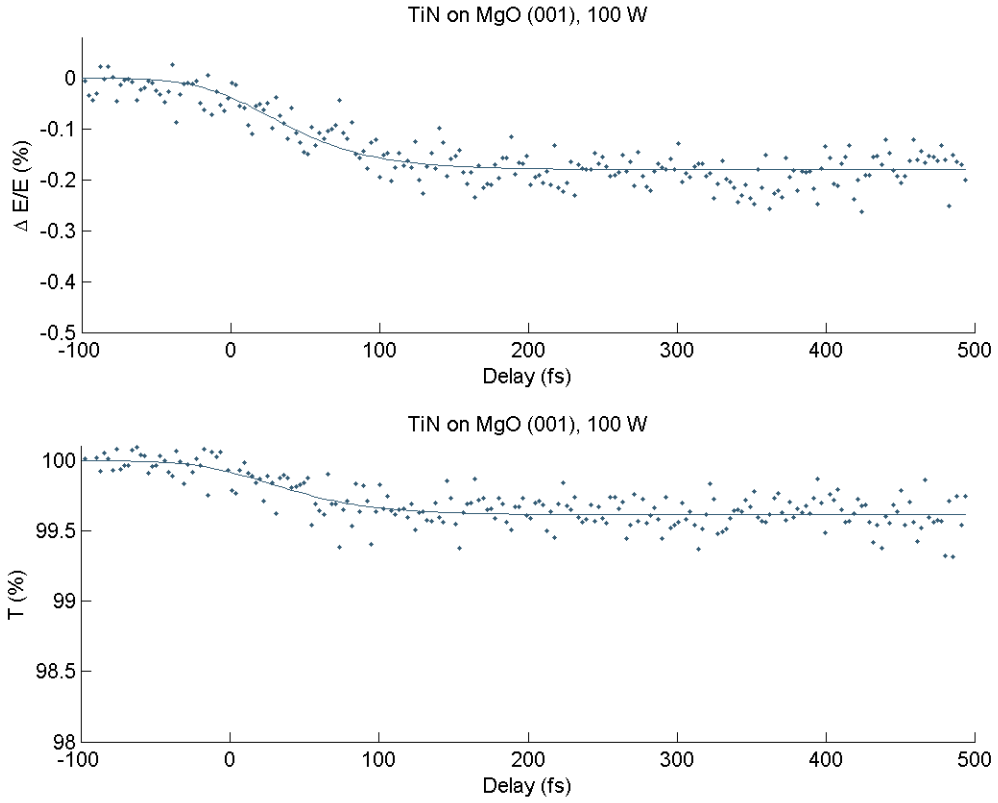

Figure 4.11. Short Delay Data and Fits for TiN on MgO, 100 W, $\tau_2 = 97ps$, $I = 36GW/cm^2$

The data points in Figure 4.12 show the collected data of $\Delta E/E$ and transmission data for the TiN on MgO, 100 W sample, for pump intensity $I = 46GW/cm^2$. The solid line in Figure 4.12 shows the expected values of $\Delta E/E$ and transmission when the nonlinear index of refraction $n_{2,\tau_2} = -16$ [E-14 m^2/W] and the nonlinear absorption coefficient $\alpha_{2,\tau_2} = 10$ [E-7 m/W]. Figure 4.12 shows that these values accurately model the collected data. The noise in the data from Figure 4.12 indicates an uncertainty of $n_{2,\tau_2} \pm 5$ [E-14 m^2/W] and $\alpha_{2,\tau_2} \pm 5$ [E-7 m/W].

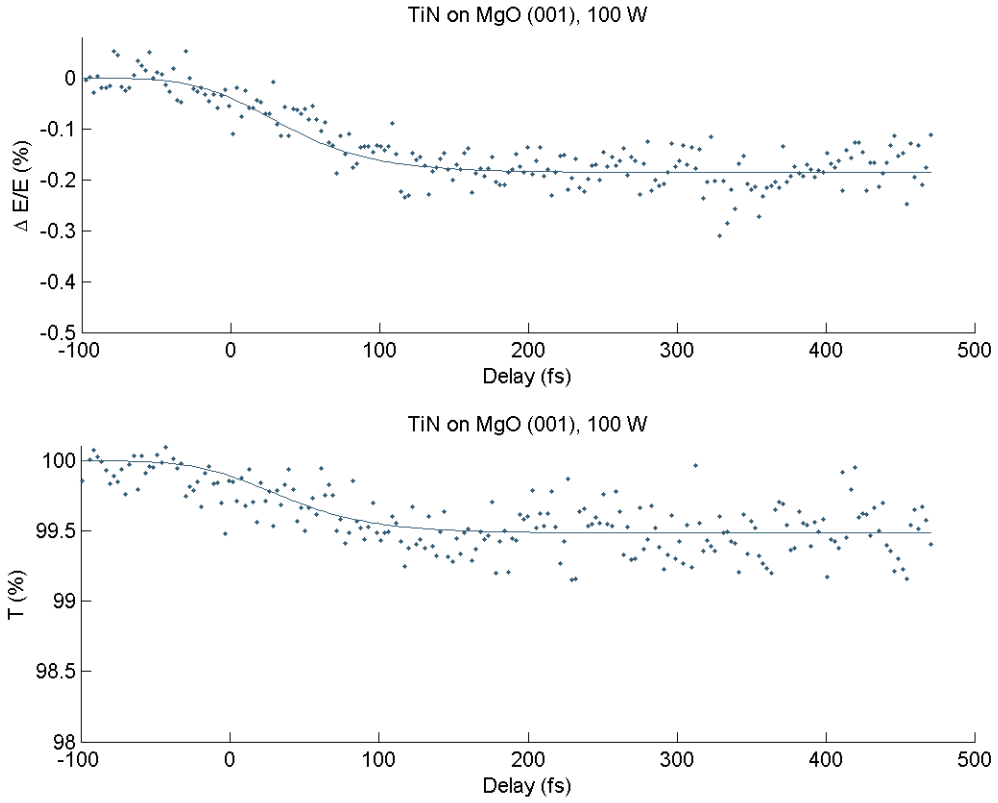

Figure 4.12. Short Delay Data and Fits for TiN on MgO, 100 W, $\tau_2 = 97ps$, $I = 46GW/cm^2$

The data points in Figure 4.13 show the collected data of $\Delta E/E$ and transmission data for the TiN on MgO, 100 W sample, for pump intensity $I = 65GW/cm^2$. The solid line in Figure 4.13 shows the expected values of $\Delta E/E$ and transmission when the nonlinear index of refraction $n_{2,\tau_2} = -16$ [E-14 m^2/W] and the nonlinear absorption coefficient $\alpha_{2,\tau_2} = 9.0$ [E-7 m/W]. Figure 4.13 shows that these values accurately model the collected data. The noise in the data from Figure 4.13 indicates an uncertainty of $n_{2,\tau_2} \pm 6.0$ [E-14 m^2/W] and $\alpha_{2,\tau_2} \pm 6.0$ [E-7 m/W].

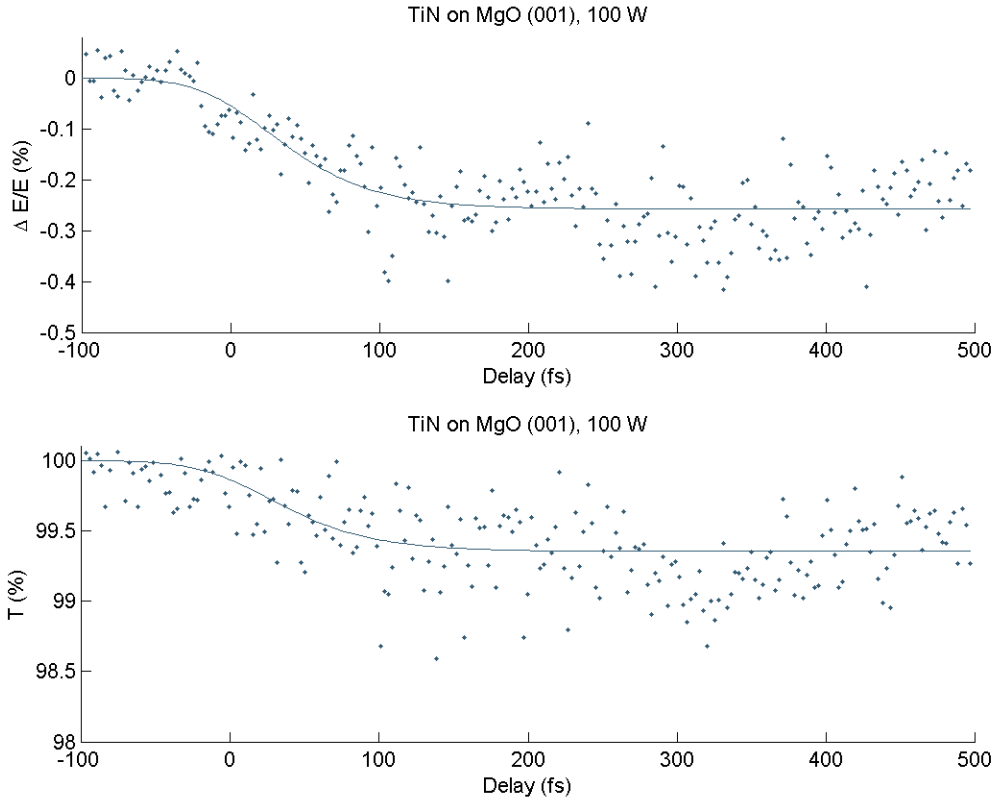

Figure 4.13. Short Delay Data and Fits for TiN on MgO, 100 W, $\tau_2 = 97ps$, $I = 65GW/cm^2$

4.3.4 NLO Properties of Nanosecond Long Decay

Figures 4.14 and 4.15 present the beam deflection results on the 600 fs time scale for the TiN on MgO, 50 W thin film.

The data points in Figure 4.14 show the collected data of $\Delta E/E$ and transmission data for the TiN on MgO, 50 W sample, for pump intensity $I = 44GW/cm^2$. The solid line in Figure 4.14 shows the expected values of $\Delta E/E$ and transmission when the nonlinear index of refraction $n_{2,\tau_2} = -36$ [E-14 m^2/W] and the nonlinear absorption coefficient $\alpha_{2,\tau_2} = 20$ [E-7 m/W]. Figure 4.14 shows that these values accurately model the collected data. The noise in the data from Figure 4.14 indicates an uncertainty of $n_{2,\tau_2} \pm 6$ [E-14 m^2/W] and $\alpha_{2,\tau_2} \pm 8$ [E-7 m/W].

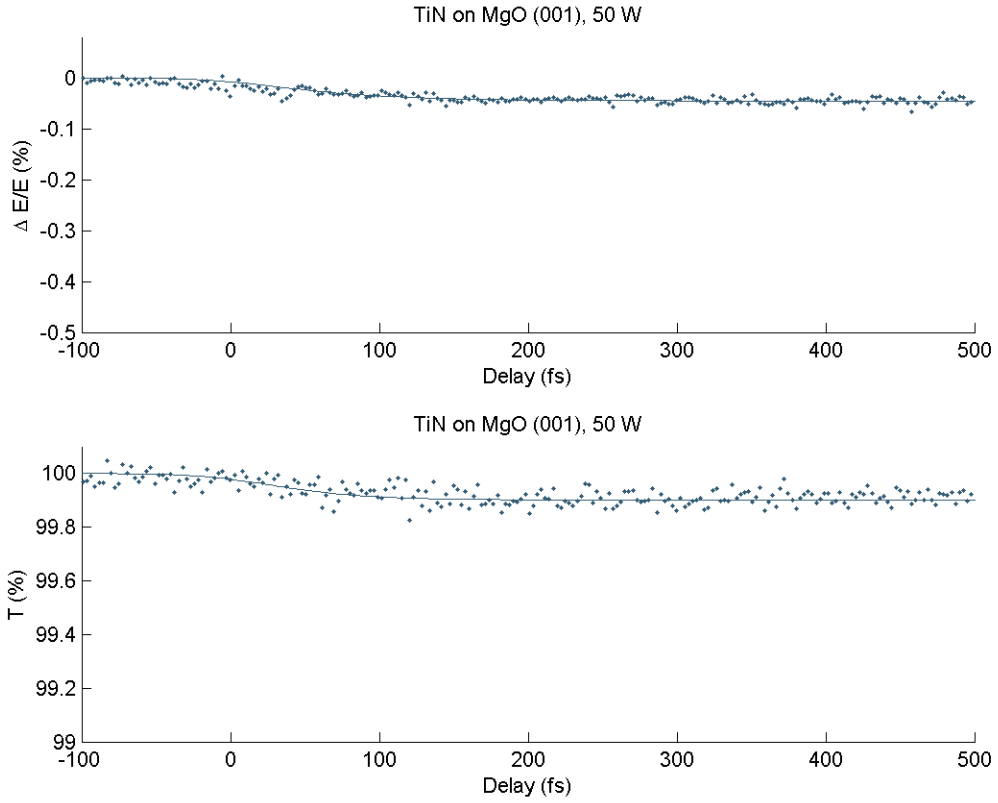

Figure 4.14. Short Delay Data and Fits for TiN on MgO, 50 W, $\tau_2 = 1.1ns$, $I = 44GW/cm^2$

The data points in Figure 4.15 show the collected data of $\Delta E/E$ and transmission data for the TiN on MgO, 50 W sample, for pump intensity $I = 69GW/cm^2$. The solid line in Figure 4.15 shows the expected values of $\Delta E/E$ and transmission when the nonlinear index of refraction $n_{2,\tau_2} = -50$ [E-14 m^2/W] and the nonlinear absorption coefficient $\alpha_{2,\tau_2} = 24$ [E-7 m/W]. Figure 4.15 shows that these values accurately model the collected data. The noise in the data from Figure 4.15 indicates an uncertainty of $n_{2,\tau_2} \pm 8$ [E-14 m^2/W] and $\alpha_{2,\tau_2} \pm 6$ [E-7 m/W].

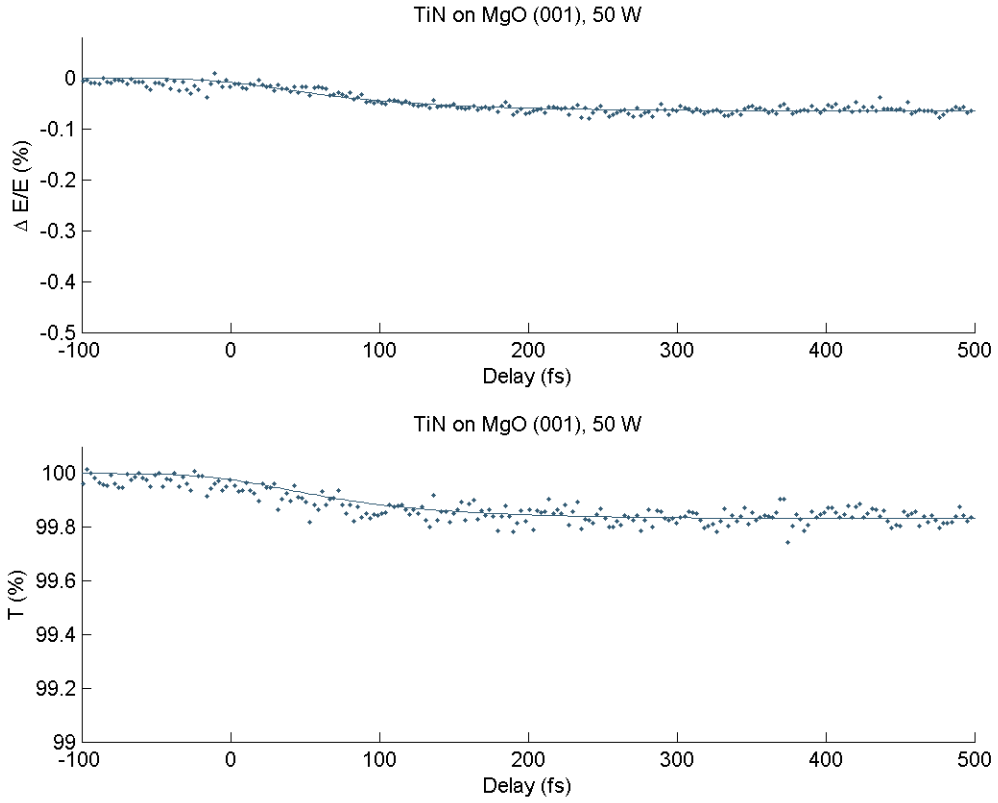

Figure 4.15. Short Delay Data and Fits for TiN on MgO, 50 W, $\tau_2 = 1.1ns$, $I = 69GW/cm^2$

Figures 4.16 and 4.17 present the beam deflection results on the 600 fs time scale for the TiN on Al_2O_3, 50 W thin film.

The data points in Figure 4.16 show the collected data of $\Delta E/E$ and transmission data for the TiN on Al_2O_3, 50 W sample, for pump intensity $I = 44GW/cm^2$. The solid line in Figure 4.16 shows the expected values of $\Delta E/E$ and transmission when the nonlinear index of refraction $n_{2,\tau_2} = -52$ [E-14 m^2/W] and the nonlinear absorption coefficient $\alpha_{2,\tau_2} = 26$ [E-7 m/W]. Figure 4.16 shows that these values accurately model the collected data. The noise in the data from Figure 4.16 indicates an uncertainty of $n_{2,\tau_2} \pm 10$ [E-14 m^2/W] and $\alpha_{2,\tau_2} \pm 8$ [E-7 m/W].

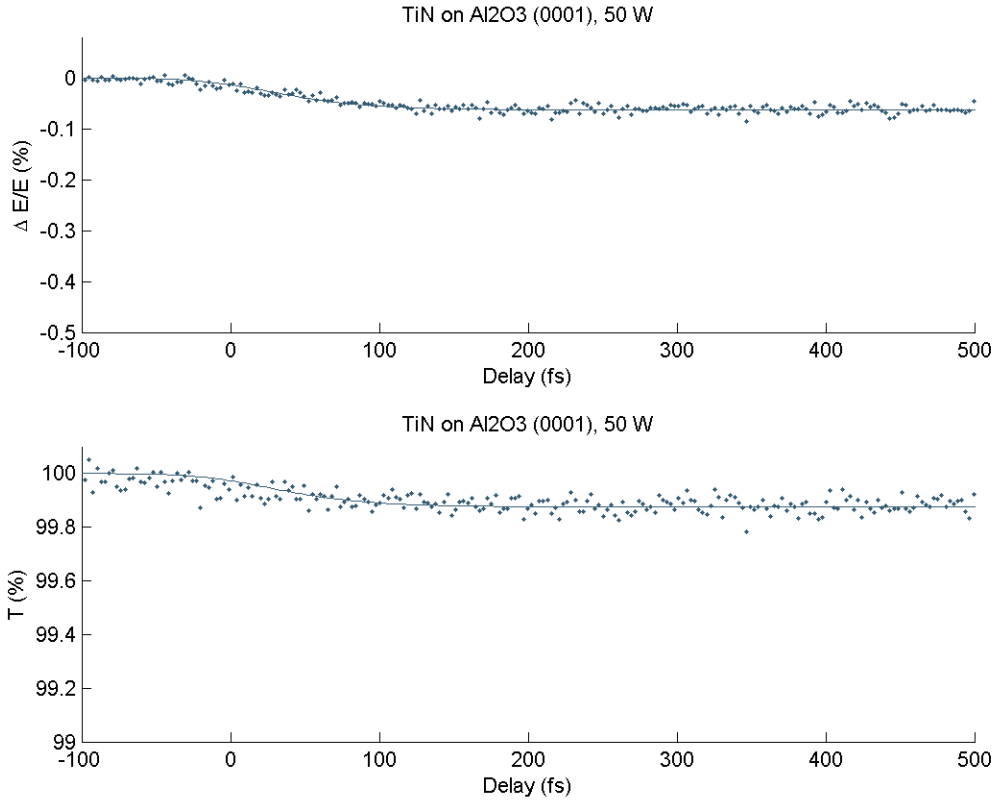

Figure 4.16. Short Delay Data and Fits for TiN on Al_2O_3, 50 W, $\tau_2 = 1.1ns$, $I = 44GW/cm^2$

The data points in Figure 4.17 show the collected data of $\Delta E/E$ and transmission data for the TiN on Al_2O_3, 50 W sample, for pump intensity $I = 69GW/cm^2$. The solid line in Figure 4.17 shows the expected values of $\Delta E/E$ and transmission when the nonlinear index of refraction $n_{2,\tau_2} = -54$ [E-14 m^2/W] and the nonlinear absorption coefficient $\alpha_{2,\tau_2} = 26$ [E-7 m/W]. Figure 4.17 shows that these values accurately model the collected data. The noise in the data from Figure 4.17 indicates an uncertainty of $n_{2,\tau_2} \pm 12$ [E-14 m^2/W] and $\alpha_{2,\tau_2} \pm 6$ [E-7 m/W].

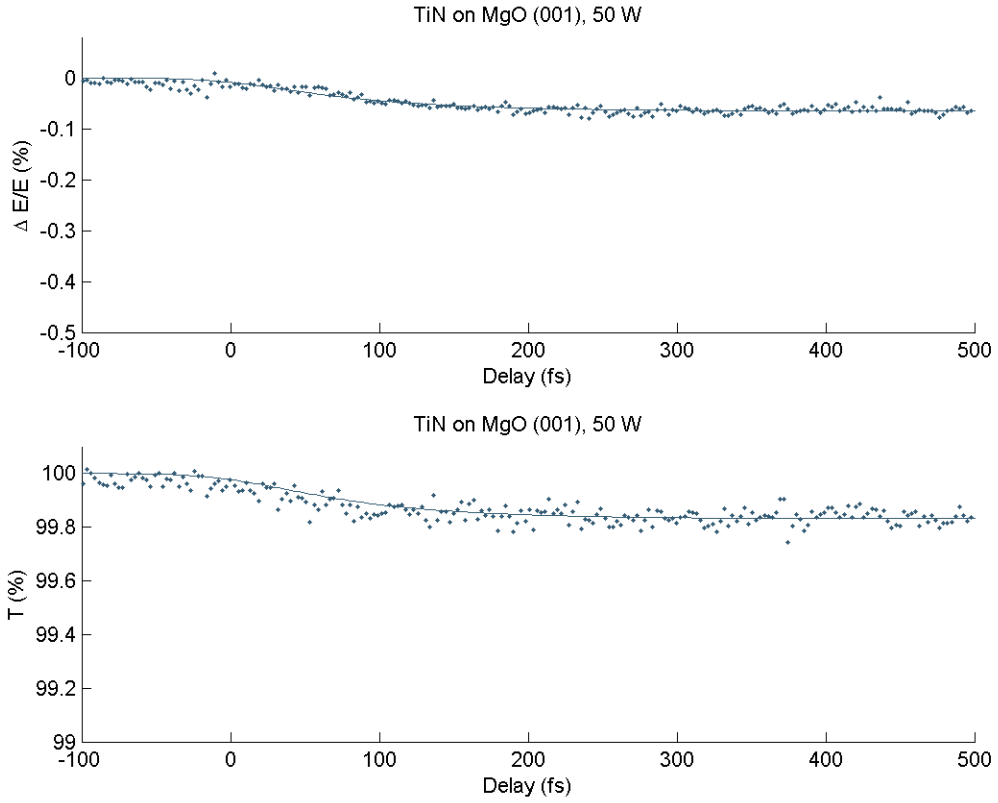

Figure 4.17. Short Delay Data and Fits for TiN on MgO, 50 W, $\tau_2 = 1.1ns$, $I = 69GW/cm^2$

Figures 4.18,4.19 and 4.20 present the beam deflection results on the 600 fs time scale for the TiN on Mgo, 100 W thin film.

The data points in Figure 4.18 show the collected data of $\Delta E/E$ and transmission data for the TiN on MgO, 100 W sample, for pump intensity $I = 36GW/cm^2$. The solid line in Figure 4.18 shows the expected values of $\Delta E/E$ and transmission when the nonlinear index of refraction $n_{2,\tau_2} = -120$ [E-14 m^2/W] and the nonlinear absorption coefficient $\alpha_{2,\tau_2} = 55$ [E-7 m/W]. Figure 4.18 shows that these values accurately model the collected data. The noise in the data from Figure 4.18 indicates an uncertainty of $n_{2,\tau_2} \pm 40$ [E-14 m^2/W] and $\alpha_{2,\tau_2} \pm 35$ [E-7 m/W]. This noise is larger than the noise for other samples. The noise in beam deflection measurements is dependent on the alignment of the experiment, not the physics of the sample.

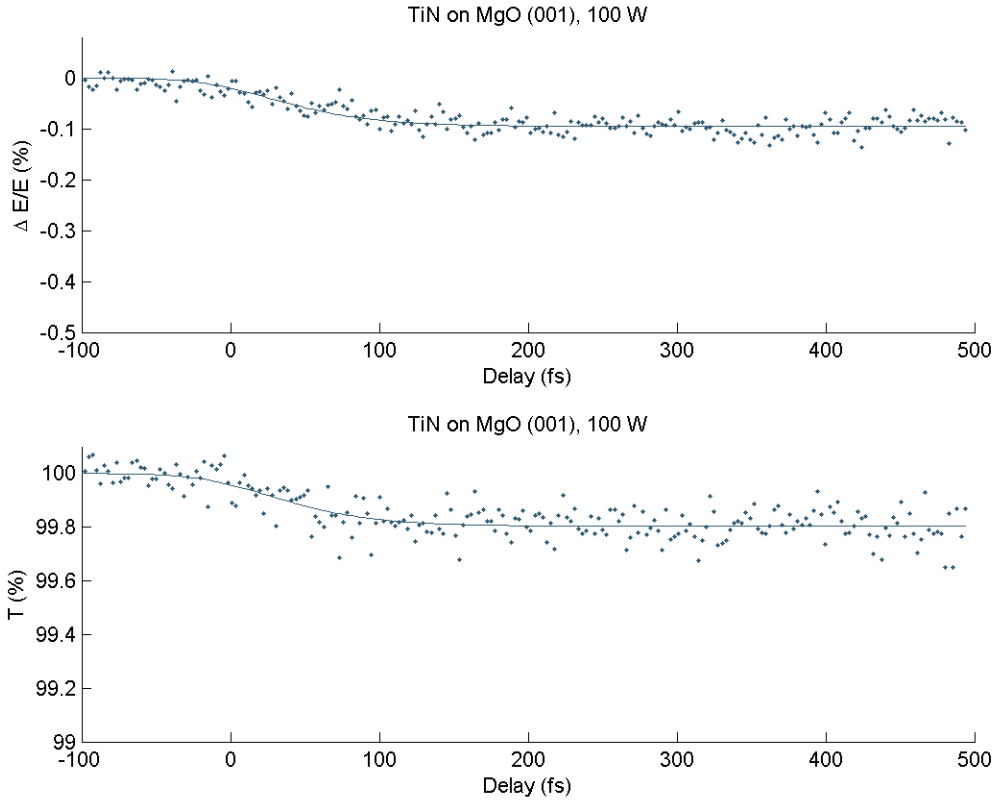

Figure 4.18. Short Delay Data and Fits for TiN on MgO, 100 W, $\tau_2 = 1.1ns$, $I = 36GW/cm^2$

The data points in Figure 4.19 show the collected data of $\Delta E/E$ and transmission data for the TiN on MgO, 100 W sample, for pump intensity $I = 46GW/cm^2$. The solid line in Figure 4.19 shows the expected values of $\Delta E/E$ and transmission when the nonlinear index of refraction $n_{2,\tau_2} = -90$ [E-14 m^2/W] and the nonlinear absorption coefficient $\alpha_{2,\tau_2} = 55$ [E-7 m/W]. Figure 4.19 shows that these values accurately model the collected data. The noise in the data from Figure 4.19 indicates an uncertainty of $n_{2,\tau_2} \pm 30$ [E-14 m^2/W] and $\alpha_{2,\tau_2} \pm 25$ [E-7 m/W].

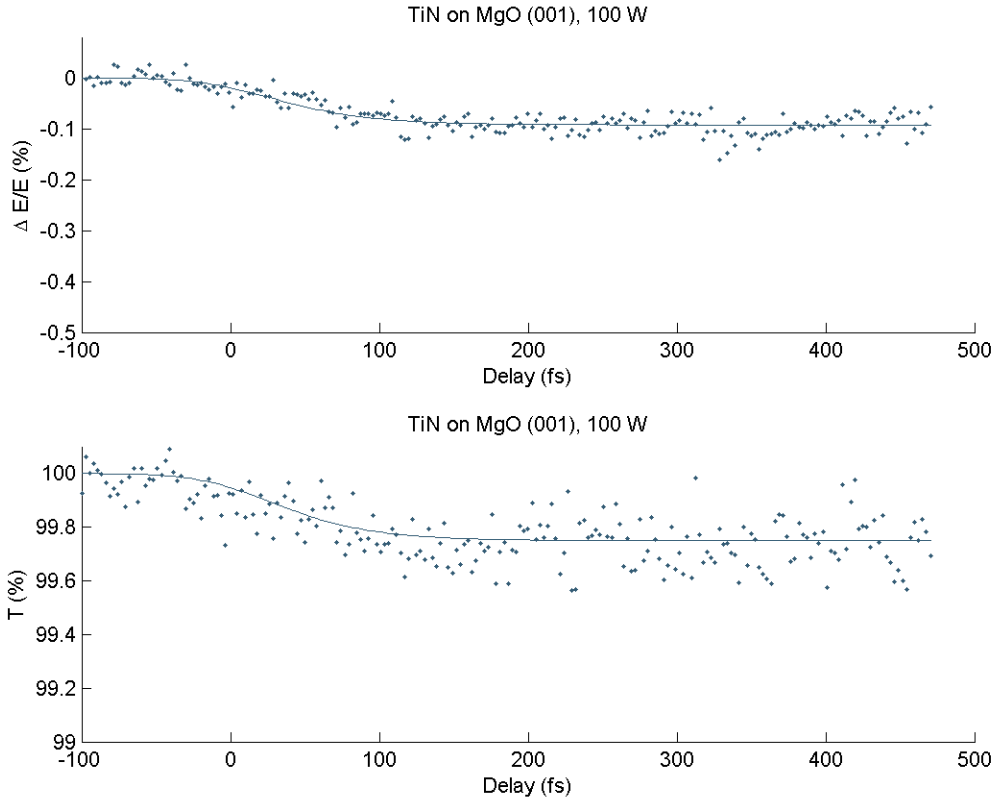

Figure 4.19. Short Delay Data and Fits for TiN on MgO, 100 W, $\tau_2 = 1.1ns$, $I = 46GW/cm^2$

The data points in Figure 4.20 show the collected data of $\Delta E/E$ and transmission data for the TiN on MgO, 100 W sample, for pump intensity $I = 65GW/cm^2$. The solid line in Figure 4.20 shows the expected values of $\Delta E/E$ and transmission when the nonlinear index of refraction $n_{2,\tau_2} = -90$ [E-14 m^2/W] and the nonlinear absorption coefficient $\alpha_{2,\tau_2} = 55$ [E-7 m/W]. Figure 4.20 shows that these values accurately model the collected data. The noise in the data from Figure 4.20 indicates an uncertainty of $n_{2,\tau_2} \pm 30$ [E-14 m^2/W] and $\alpha_{2,\tau_2} \pm 25$ [E-7 m/W].

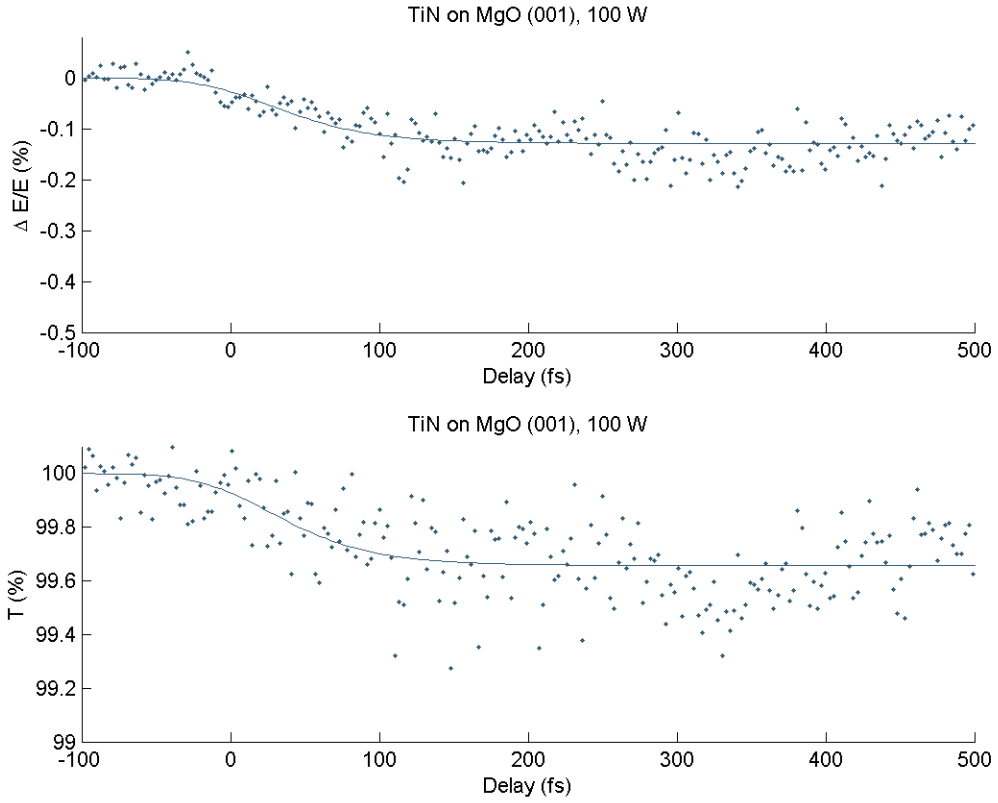

Figure 4.20. Short Delay Data and Fits for TiN on MgO, 100 W, $\tau_2 = 1.1ns$, $I = 65GW/cm^2$

4.3.5 Comparisons

Figures 4.21 and 4.22 present the n_{2,τ_1} and α_{2,τ_1},found in Section 4.3.3, for each sample at each intensity.

Comparing TiN on MgO, 50 W (top) to TiN on Al_2O_3, 50 W (middle), contributes to objective 2. The NLO property n_{2,τ_1} is not significantly altered by changing the substrate from MgO to Al_2O3. The NLO property α_{2,τ_1} is not significantly altered by changing the substrate from MgO to Al_2O_3.

Comparing TiN on MgO, 50 W (top) to TiN on MgO, 100 W (bottom), contributes to objective 3. The NLO property n_{2,τ_1} may be altered by changing the deposition power from 50 W to 100 W. There is not enough evidence to conclude

that α_{2,τ_1} is significantly altered by changing the deposition power from 50 W to 100 W. Increasing the precision of the beam deflection measurements, by reducing noise in the measurements, would be useful.

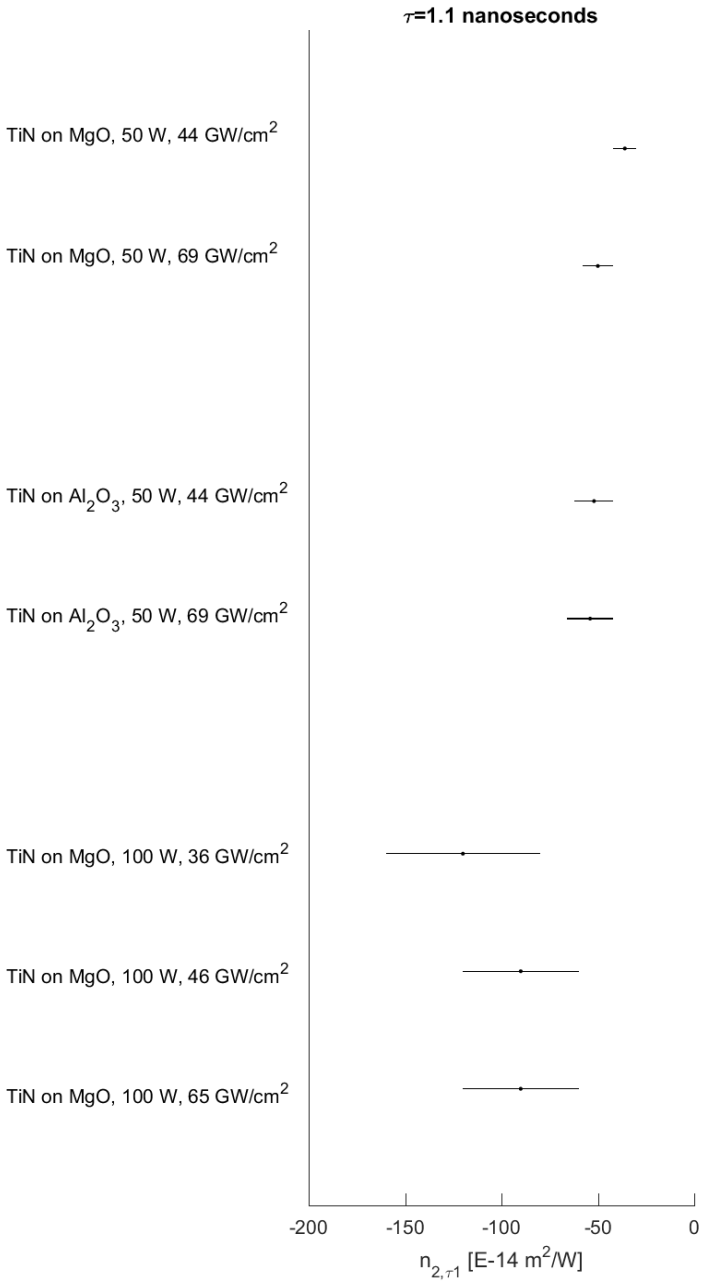

Figure 4.21. n_{2,τ_1} **for each sample**

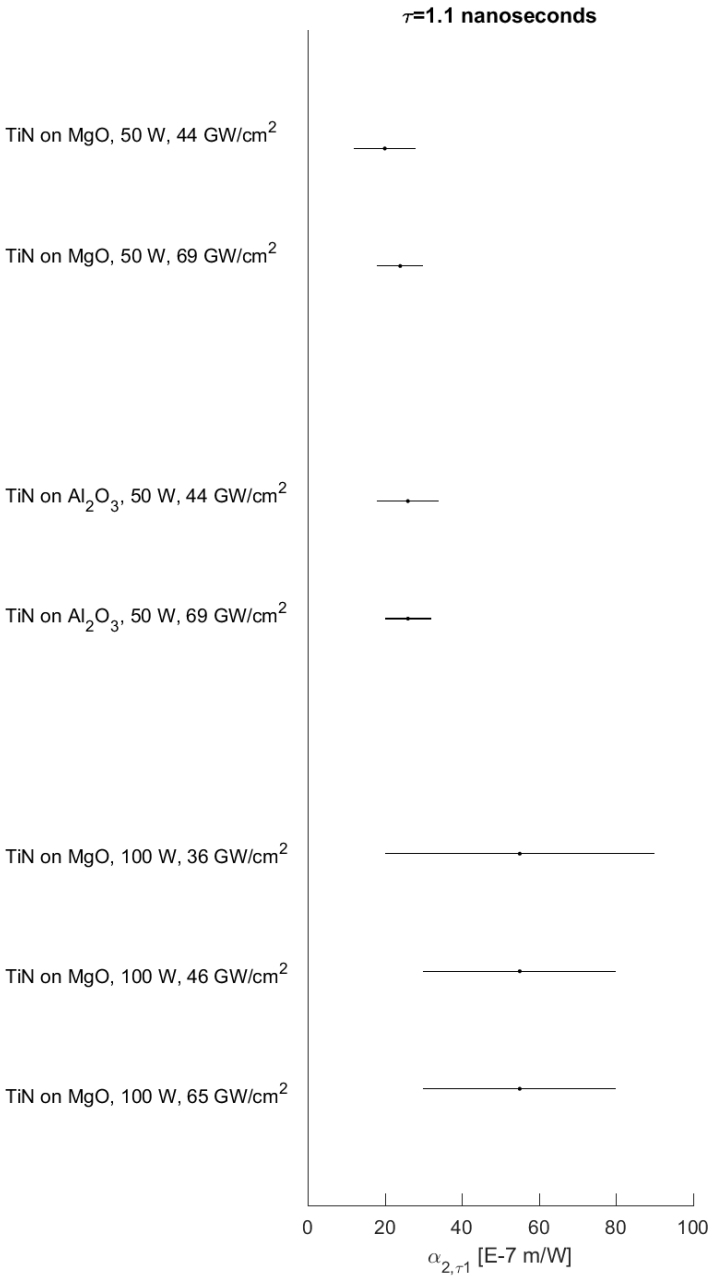

Figure 4.22. α_{2,τ_1} **for each sample**

Figures 4.23 and 4.24 present the n_{2,τ_2} and α_{2,τ_2},found in Section 4.3.4, for each sample at each intensity.

Comparing TiN on MgO, 50 W (top) to TiN on Al_2O_3, 50 W (middle), contributes to objective 2. The NLO property n_{2,τ_2} is not significantly altered by changing the substrate from MgO to Al_2O_3. The NLO property α_{2,τ_2} is not significantly altered by changing the substrate from MgO to Al_2O_3.

Comparing TiN on MgO, 50 W (top) to TiN on MgO, 100 W (bottom), contributes to objective 3. The NLO property n_{2,τ_2} may be altered by changing the deposition power from 50 W to 100 W. There is not enough evidence to conclude that α_{2,τ_2} is altered by changing the deposition power from 50 W to 100 W. Increasing the precision of the beam deflection measurements, by reducing noise in the measurements, would be useful.

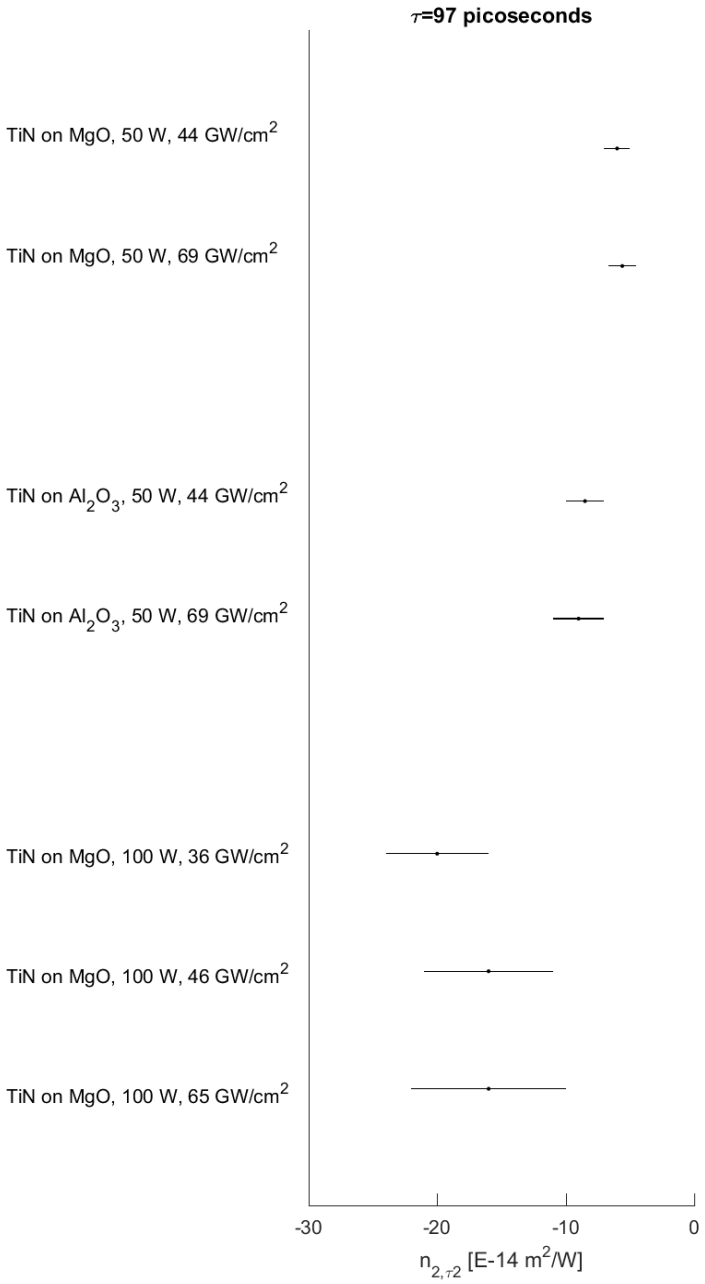

Figure 4.23. n_{2,τ_2} **for each sample**

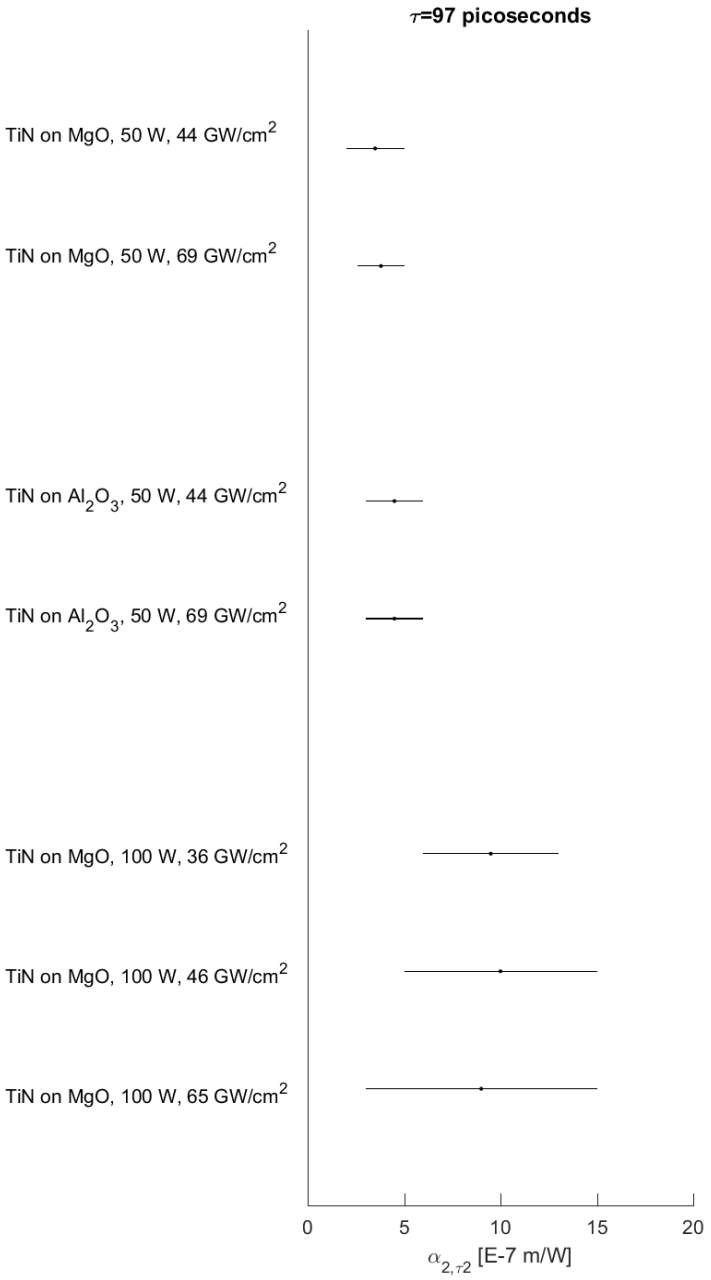

Figure 4.24. α_{2,τ_2} **for each sample**

To summarize, neither n_2 nor α_2, for either electron-electron or electron-phonon relaxation, is altered by substrate. There is evidence that n_2, for both values electron-electron and electron-phonon relaxation, may be altered by deposition power. There is not enough evidence that α_2, for both values electron-electron and electron-phonon relaxation, may be altered by deposition power.

V. Conclusions and Recommendations

5.1 Objectives

Objective 1, to measure the time dynamics of the NLO properties of TiN, has been met. The thin film TiN samples exhibit no electronic response. The samples exhibit long decays opposite in sign to the substrate's electronic response. This response is indicative of hot electrons, also called carrier heating. In fact, the response is consistent with the two temperature model of electron-electron and electron-phonon coupling. A band gap renormalization response, which would be indicative of semiconductor behavior, is absent from all samples. Taken together, the time dynamics of the NLO properties indicate that TiN behaves as a metal.

Table 5.1. Summary of NLO properties, fit with $\tau_1 = 1.1ns$ and $\tau_2 = 97ps$

	α_{2,τ_1}	[E-7 $\frac{m}{W}$]	n_{2,τ_1}	[E-14 $\frac{m^2}{W}$]	α_{2,τ_2}	[E-7 $\frac{m}{W}$]	n_{2,τ_2}	[E-14 $\frac{m^2}{W}$]
TiN on MgO 50 W	22	± 8.0	-43	± 8.0	3.7	± 1.5	-5.8	± 1.1
TiN on Al_2O_3 50 W	26	± 8.0	-53	± 12	4.5	± 1.5	-8.8	± 2.0
TiN on MgO 100 W	55	± 35	-100	± 40	9.5	± 6.0	-17	± 6.0

Objective 2, to measure the effect of substrate on the NLO properties of TiN, has been met. While there is not enough evidence to conclude that the difference between MgO and Al_2O_3 has an effect on the NLO propertied of thin film TiN, comparing these results with that of Reed et al. suggests that the NLO properties are tunable by substrate. While films measured in this research are all epitaxial growth, the films measured by Reed et al. were not.

The dissimilarities between TiN grown on MgO and Al_2o_3, specifically TiN orientation and lattice matching, are insignificant to the NLO properties. However, the dissimilarities between epitaxial and non-epitaxial may be significant to the NLO properties of the thin film. There will be more crystal boundaries, which would impede the long decay mechanisms, in TiN on fused silica than in TiN on MgO or

Al_2o_3. Therefor, it is consistent with the underlying physical mechanisms that short delay mechanisms will dominate the response in the TiN on fused silica, and long delay mechanisms will dominate the response in the TiN on MgO or Al_2o_3.

The comparison of these two results, while consistent with underlying physical mechanisms, is not enough to conclude that the NLO properties are tunable by substrate. The films were made by different methods. In order to confirm that the differences in transient NLO dynamics are the result of substrate, thin film TiN may be grown on fused silica by the same method used in this research (controllably unbalanced reactive magnetron sputtering), and the NLO properties compared to the results presented here.

Objective 3, to measure the effect of deposition power on the NLO properties of TiN, has been met. There is evidence that deposition power has an effect on n_2. As seen in the AFM in Appendix A, the 50 W and 100 W films are very similar, but there is some difference in film quality.

5.2 Motivation

Returning to the motivation discussed in Section 1.4, TiN is not a perfect material for imaging protection nor all optical computing. TiN has the large magnitude and long response NLO properties desirable for imaging protection, but also has large linear absorption. An ideal material would have very small linear absorption, so as to not interfere with the imaging equipment during normal operation. TiN has the large magnitude NLO properties desirable for all optical computing, but the response is entirely long decay, not short decay. As the decay in inversely related to the frequency of the computing, this is not ideal. Perhaps TiN could still be used in an optical computer, but not as the switching material.

5.3 Recommendations for Future Research

5.3.1 Further possibility of Tuning TiN

Returning to the list of factors effecting material properties discussed in Section 2.4, the NLO properties thin film TiN may be tunable by chemical composition, crystal structure or defect structure. Nonstoichiometric TiN may have different NLO properties. Since the stoichiometric TiN investigated in this work has very metallic properties, the suggested direction of study would be a higher concentration of Nitrogen. The difference in defect structure was not significant between TiN on MgO and TiN on Al_2O_3, but may be significant for TiN on fused silica. Using controllably unbalanced reactive magnetron sputtering to grow TiN on fused silica is a possible avenue of research. Impurity concentration, such as oxidation, was not discussed in this work and is another possible avenue of research.

5.3.2 Other Nitrides

Other nitrides will have significantly different NLO properties. While TiN had metallic properties, as expected, Scandium nitride (ScN) is expected to have semiconducting properties and aluminum nitride (AlN) is expected to have insulating properties. These assertions should be verified, and then tunability can be developed by alloying and layering these materials.

5.3.3 Two Temperature Models

Applying a biexponential fit to the relaxation of the NLO properties attempts to account for the electron-electron and electron-phonon coupling included in two temperature models. While this is an improvement over the simpler exponential models used in the past, it is still an oversimplification of existing phenomenological and semiclassical two temperature models. Both the phenomenological model developed

by Jiang et al. [11] and the semiclassical model developed by Chen et al. [2] are applied to gold thin films. The relaxation times found in this work, 97ps and 1.1ns, are consistent with these models, which predict relaxation times longer than 10 to 16 picoseconds. However, to truly incorporate either model into fitting the data collected in this work, the models would need to be applied to TiN.

5.4 Conclusions

The objectives of the research were met. Thin film TiN has metallic NLO properties. These properties are not tunable by changing the substrate from MgO to Al_2O_3. These properties may be tunable by manipulating film quality by changing the deposition power. In the future, the beam deflection technique should be used to measure the NLO properties of ScN and AlN, along with alloys and layers of these materials. The biexponential fit better represents the electron-electron and electron-phonon coupling mechanisms than the previously used single exponential. To further improve this representation, a two temperature model should be applied to TiN and used to fit the beam deflection results.

Appendix A. Material Characterization

A.1 Ellipsometry

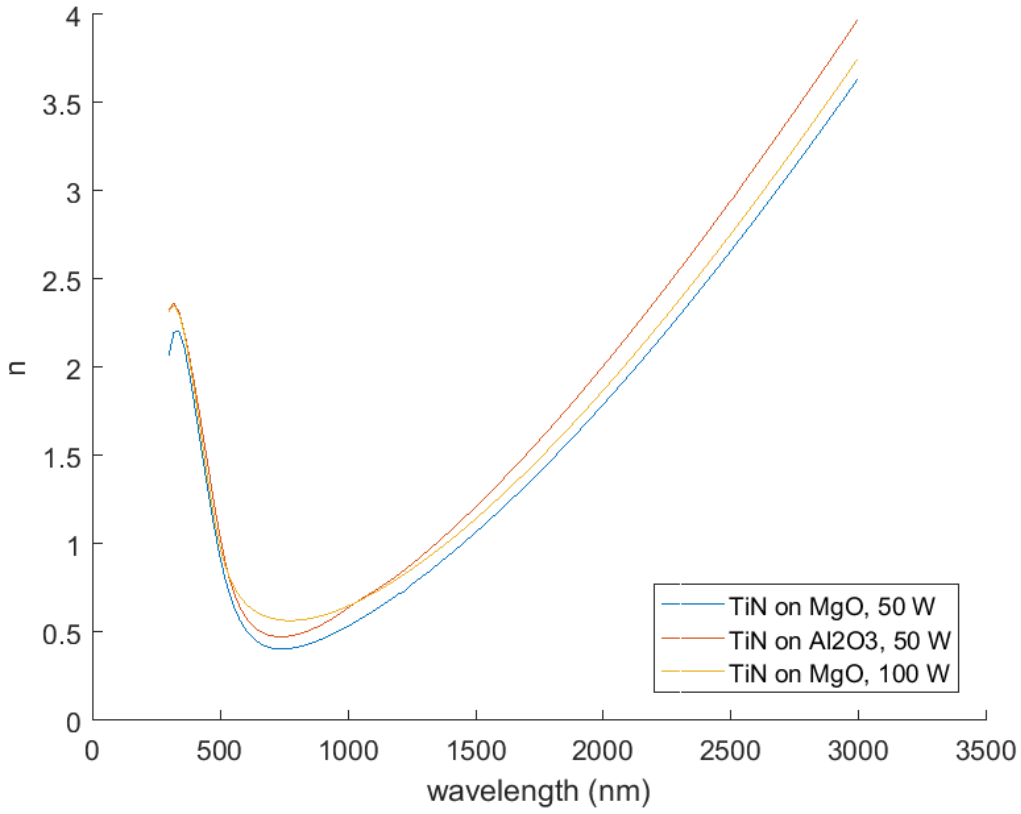

Figure A.1. Ellipsometry results for all samples, n

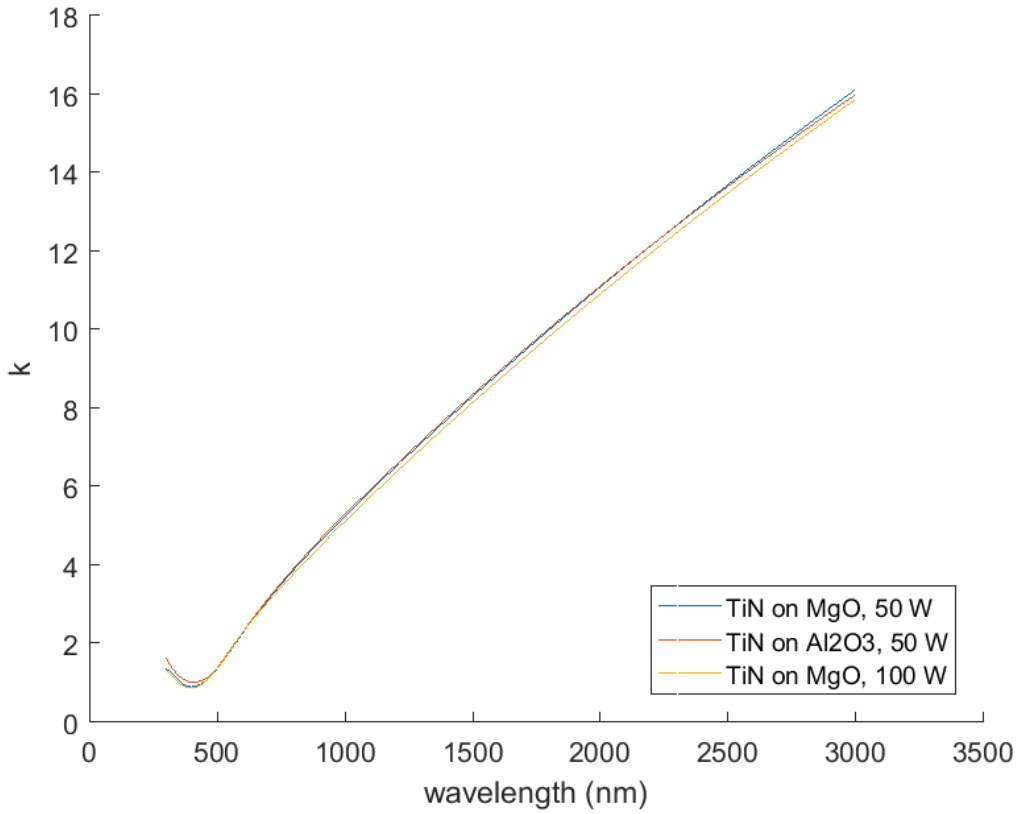

Figure A.2. Ellipsometry results for all samples, k

A.2 Atomic Force Microscopy

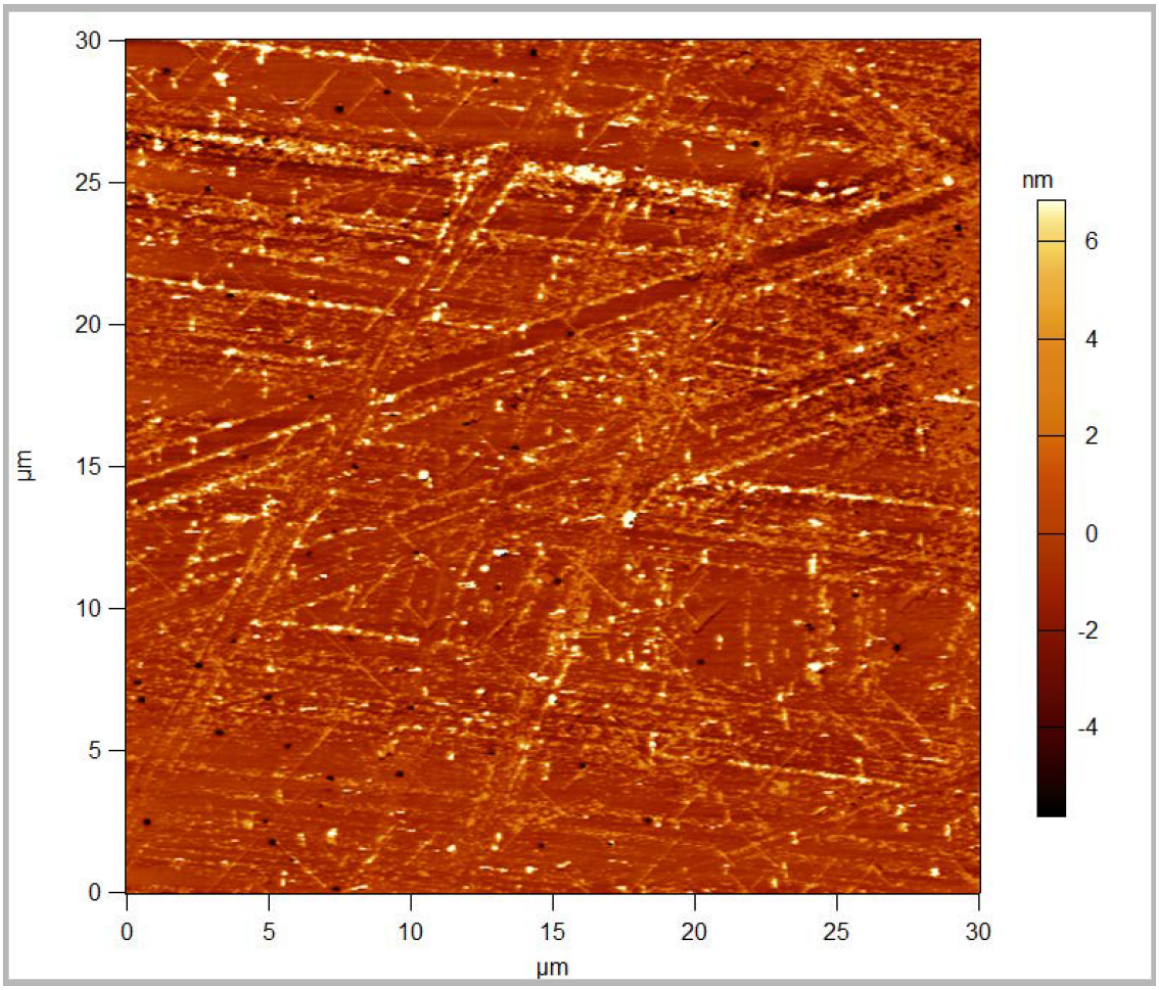

Figure A.3. AFM for TiN on MgO, 50 W

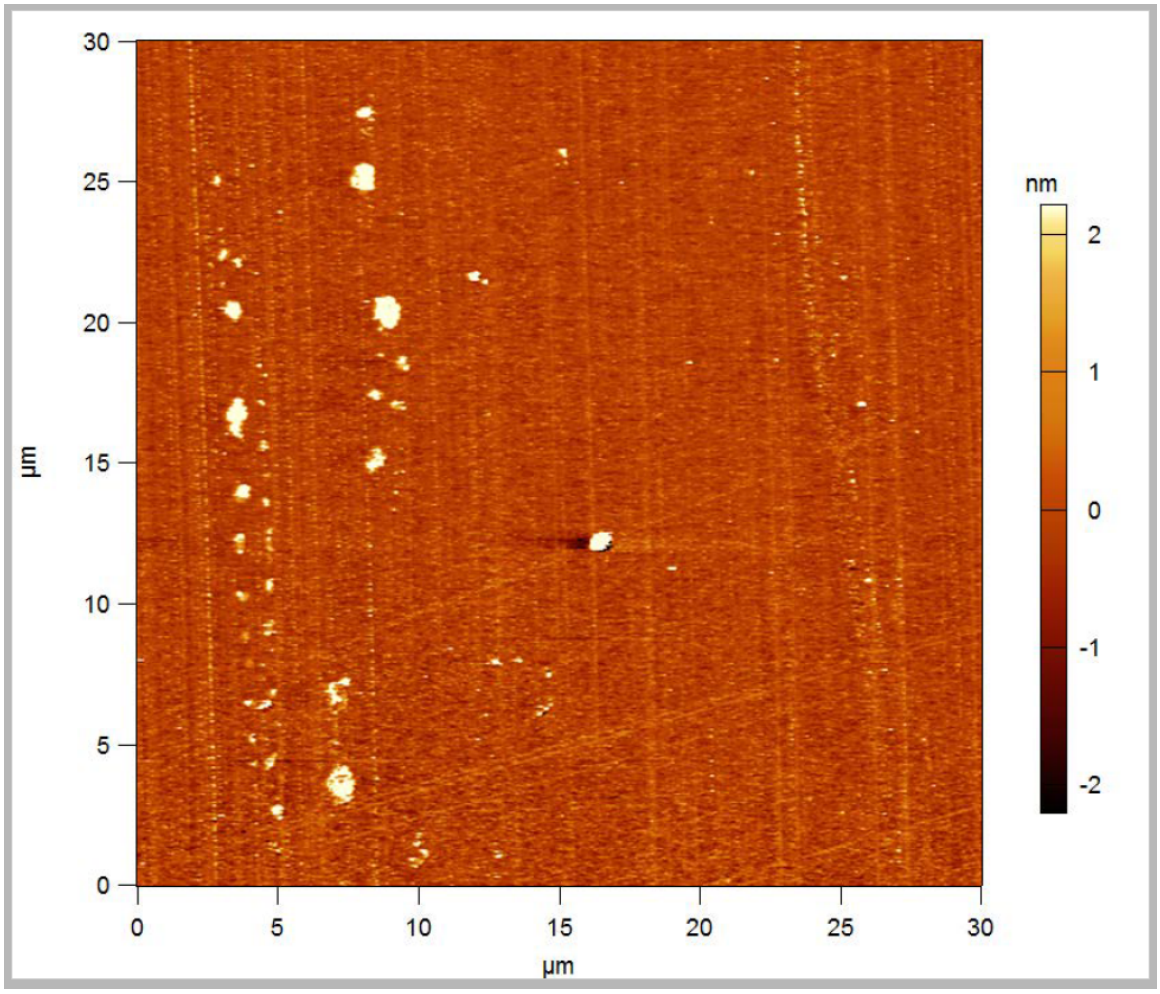

Figure A.4. AFM for TiN on Al_2O_3, 50 W

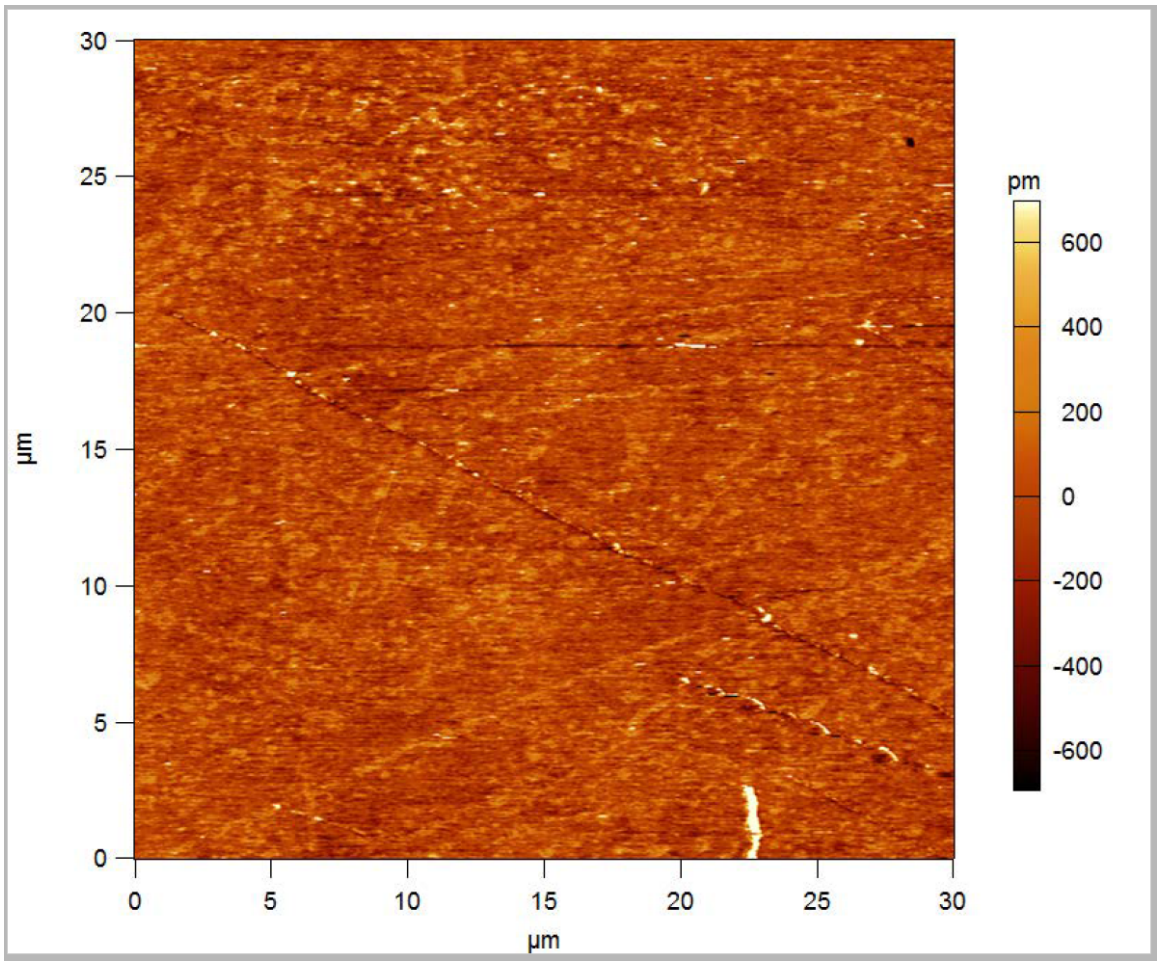

Figure A.5. AFM for TiN on MgO, 100 W

Bibliography

[1] E. W. VanStryland *et al.*, "Optical limiting with semiconductors," vol. 5, no. 9, pp. 1980–1988, 1988.

[2] J. Chen *et al.*, "A semiclassical two-temperature model for ultrafast laser heating," *International Journal of Heat and Mass Transfer*, vol. 49, pp. 307–316, 2006.

[3] D. Christodoulides *et al.*, "Nonlinear refraction and absorption: mechanisms and magnitudes," *Adv. Opt. Photon.*, vol. 2, no. 1, pp. 60–200, 2010. [Online]. Available: http://aop.osa.org/abstract.cfm?URI=aop-2-1-60

[4] M. Ferdinandus, "Techniques For Characterization Of Third Order Optical Nonlinearities," Ph.D. dissertation, 2014.

[5] J. Reed *et al.*, "Transient nonlinear refraction measurements of titanium nitride thin films," 2016.

[6] P. Leclair, "Titanium Nitride Thin Films by the Electron Shower Process," *Departmen t of Materials Science and Engineering MIT*, 1998.

[7] M. R. Ferdinandus, "Plasmonic Nanostructures for All-Optical Signal Processing," no. 937, 2015.

[8] "Federal contract opportunity baa-afrl-rqks-2016-0010."

[9] B. Saleh and M. C. Teich, *Fundamentals of Photonics*, 2nd ed. Wiley, 2007.

[10] R. W. Boyd, *Nonlinear Optics*, 3rd ed. Elsevier, 2008.

[11] L. Jiang and H. lung Tsai, "Improved Two-Temperature Model and Its Application in Ultrashort Laser Heating," *Journal of Heat Transfer*, vol. 127, no. October 2005, pp. 1167–1173, 2017.

[12] M. Bonn *et al.*, "Ultrafast electron dynamics at metal surfaces : Competition between electron-phonon coupling and hot-electron transport," vol. 61, no. 2, pp. 1101–1105, 2000.

[13] L. Toth, *Transition Metal Carbides and Nitrides*, 1st ed. New York, NY: Academic Press, Inc., 1971.

[14] S. Oyama, *The Chemistry of Transition Metal Carbides and Nitrides*, 1st ed. Chapman and Hall, 1996.

[15] E. Valkonen *et al.*, "Optical constants of thin TiN films: thickness and preparation effects," pp. 3624–3630, 1986.

[16] Z.-y. Yang *et al.*, "Room temperature fabrication of titanium nitride thin films as plasmonic materials by high-power impulse magnetron sputtering," vol. 6, no. 2, pp. 2230–2239, 2016.

[17] M. Wall *et al.*, "Nucleation kinetics during homoepitaxial growth of TiN(001) by reactive magnetron sputtering," *Physical Review B*, vol. 70, no. 3, pp. 1–8, 2004.

[18] N. Kinsey *et al.*, "Effective Third-Order Nonlinearities in Refractory Plasmonic TiN Thin Films," 2016.

REPORT DOCUMENTATION PAGE

Form Approved
OMB No. 0704-0188

1. REPORT DATE *(DD-MM-YYYY)*	**2. REPORT TYPE**	**3. DATES COVERED** *(From - To)*
23 Mar 2017	Master's Thesis	01 Sept 2015 — 23 Mar 2017

4. TITLE AND SUBTITLE

Transient Nonlinear Optical Properties of Thin Film Titanium Nitride

5a. CONTRACT NUMBER

5b. GRANT NUMBER

5c. PROGRAM ELEMENT NUMBER

6. AUTHOR(S)

Thomas, SarahKatie

5d. PROJECT NUMBER
17P224

5e. TASK NUMBER

5f. WORK UNIT NUMBER

7. PERFORMING ORGANIZATION NAME(S) AND ADDRESS(ES)

Air Force Institute of Technology
Graduate School of Engineering and
Management (AFIT/EN)
2950 Hobson Way
WPAFB OH 45433-7765

8. PERFORMING ORGANIZATION REPORT NUMBER

AFIT-ENP-MS-17-M-106

9. SPONSORING / MONITORING AGENCY NAME(S) AND ADDRESS(ES)

AFOSR - Att: Dr. Kenneth Caster
875 North Randolph St
Ste 325, Room 3112
Arlington VA 22203
Email: Kenneth.caster@us.af.mil

10. SPONSOR/MONITOR'S ACRONYM(S)

AFOSR

11. SPONSOR/MONITOR'S REPORT NUMBER(S)

12. DISTRIBUTION / AVAILABILITY STATEMENT

DISTRIBUTION STATEMENT A:
APPROVED FOR PUBLIC RELEASE; DISTRIBUTION UNLIMITED.

13. SUPPLEMENTARY NOTES

14. ABSTRACT

The objective of this thesis is to measure the transient nonlinear properties of thin film transition metal nitrites, specifically titanium nitride (TiN) and scandium nitride (ScN), using the beam deflection characterization technique. The thin films were made at the Air Force Research Lab by controllably unbalanced magnetron sputtering.

Transition metal nitrides, specifically TiN, are used widely in industry because of their unique properties, including extreme hardness and high damage threshold. The properties of thin film transition metal nitrites are dependent on the chemical structure of the thin film, which can be heavily influenced by substrate and deposition method. This durability and tunability is an asset in applications such as sensor protection and all optical computing.

Two substrates, sapphire (Al_2O_3) and magnesium oxide (MgO), were investigated. Two deposition parameters, 50V and 100V, were investigated. The substrate nor deposition parameter significantly affect the nonlinear optical properties.

15. SUBJECT TERMS

Titanium nitride, nonlinear characterization, nonlinear optical properties.

16. SECURITY CLASSIFICATION OF:			**17. LIMITATION OF ABSTRACT**	**18. NUMBER OF PAGES**	**19a. NAME OF RESPONSIBLE PERSON**
a. REPORT	**b. ABSTRACT**	**c. THIS PAGE**			Maj Manuel Ferdinandus
U	U	U	UU	86	**19b. TELEPHONE NUMBER** (937) 255-3636 x4339 Manuel.ferdinandus@us.af.mil